Persistent dopamine-dependent remodeling of the neural transcriptome in response to pregnancy and postpartum

Jennifer C Chan[1], Giuseppina Di Salvo[1,2], Ashley M. Cunningham[1], Sohini Dutta[1], Elizabeth Brindley[1], Benjamin H. Weekley[1], Ethan Wan[4], Cindy Zhang[1], Naguib Mechawar[5], Gustavo Turecki[5], Ian Maze[1,3,6*]

Affiliations

[1]Nash Family Department of Neuroscience, Friedman Brain Institute, Icahn School of Medicine at Mount Sinai, New York, NY, 10029, USA

[2]Department of Psychiatry and Neuropsychology, School for Mental Health and Neuroscience (MHeNs), Maastricht University, Maastricht, The Netherlands

[3]Department of Pharmacological Sciences, Icahn School of Medicine at Mount Sinai, New York, NY, 10029, USA

[4]Department of Neurobiology, University of Alabama at Birmingham, Birmingham, AL 35294, USA.

[5]Douglas Institute, Department of Psychiatry, McGill University, Montreal, QC, Canada, H4H 1R3.

[6]Howard Hughes Medical Institute, Icahn School of Medicine at Mount Sinai, New York, NY, 10029, USA

***Corresponding author**
Ian Maze
Email: ian.maze@mssm.edu

ABSTRACT

Pregnancy and postpartum experiences represent transformative physiological states that impose lasting demands on the maternal body and brain, resulting in lifelong neural adaptations[1–6]. However, the precise molecular mechanisms driving these persistent alterations remain poorly understood. Here, we used brain-wide transcriptomic profiling to define the molecular landscape of parity-induced neural plasticity, identifying the dorsal hippocampal formation (dHF) as a key site of transcriptional remodeling. Combining single-cell RNA sequencing with a maternal-pup separation paradigm, we additionally demonstrated that chronic postpartum stress significantly disrupts dHF adaptations by altering dopamine dynamics, leading to changes in the dopamine-dependent histone post-translational modification – H3 dopaminylation, with further alterations in transcription, cellular plasticity, and behavior. In human dorsal subiculum, a brain structure within the dHF, we uncovered conserved patterns of parity-dependent alterations in H3 dopaminylation and transcription. We further established the sufficiency of dopamine modulation in regulating these parity-induced adaptations via chemogenetic suppression of dopamine release into the dHF, which recapitulated key epigenomic and behavioral features of parity in virgin female mice. In sum, our findings establish dopamine as a central regulator of parity-induced neuroadaptations in humans and mice, revealing a fundamental transcriptional mechanism by which female reproductive experiences remodel the brain to sustain long-term behavioral adaptations.

INTRODUCTION

Matrescence – the physical, emotional, hormonal, and social transition to motherhood – is a period of profound transformation that reshapes the maternal body and brain to support pregnancy, birth, and offspring care. While extensive research has focused on acute maternal brain processes that are essential for the onset and maintenance of parenting, precisely how brain adaptations are sustained beyond the postpartum period to persistently influence behavior remains unclear. Recent human neuroimaging studies have revealed that pregnancy experience induces long-lasting alterations in brain connectivity and structure, persisting for years or even decades following birth[1–6]. Animal models examining parity – the state of previously carrying a pregnancy to term – similarly have demonstrated persistent alterations in synaptic remodeling, cell proliferation, and behavioral outcomes[7–14]. However, the specific mechanisms within the extensive repertoire of maternal physiological changes that drive these long-lasting brain adaptations remain poorly understood.

Here, we employed brain-wide transcriptional profiling to systematically characterize the persistent impact of parity on the maternal brain in mice. These analyses surprisingly revealed the dorsal hippocampual formation (dHF) as a key site of sustained plasticity. We then leveraged single-cell RNA sequencing, Cleavage Under Targets and Release Using Nuclease followed by sequencing (CUT&RUN-seq), a postpartum stress paradigm, behavioral assays, chemogenetic approaches, and human brain tissue analyses to identify and validate a dopamine-dependent neuromodulatory process that orchestrates these sustained maternal adaptations. Importantly, these brain-wide datasets will also serve as a critical resource for future investigations into the reproductive state-dependent adaptations that contribute to matrescence.

RESULTS

Parity promotes long-lasting transcriptional and behavioral adaptations in maternal brain

To first investigate the persistent effects of female reproductive experiences in maternal brain, we established a timeline to compare primiparous dams (PP), which experienced breeding, pregnancy, parturition, lactation, and pup interactions, to age-matched virgins that lacked reproductive experiences (nulliparous, NP; **Fig. 1a**). Given that reproductive hormones return to baseline levels ~7-weeks post-conception[15], we conducted brain-wide transcriptomic profiling 4-weeks following cessation of pup rearing (i.e. 49 days postpartum; dpp), as this time point would be predicted to reflect sustained changes. Following differential expression analyses of 11 brain regions selected based on prior evidence supporting their involvement in maternal behaviors[16,17] (**Extended Data 1a**), our data revealed a wide-range in the number of differentially expressed genes (DEGs, adj. $p < 0.05$) across brain regions (**Fig. 1b, Extended Data Table 1**). These differences indicated varying levels of transcriptomic sensitivity to parity brain-wide, with few changes observed in the medial prefrontal cortex (mPFC), for example, as compared to the dHF, the region found to be most robustly regulated in our analyses.

To next assess whether these differential expression patterns could be attributed to changes in shared cell-types, we performed cell-type deconvolution using BRETIGEA, which compares whole transcriptome data to validated brain cell type-specific marker gene sets[18]. We observed changes in cell marker expression for neurons, astrocytes, microglia, oligodendrocyte precursor cells (OPCs), oligodendrocytes, and endothelial cells across brain regions, regardless of the number of DEGs (**Fig. 1c**). These data suggested that cellular changes may occur across brain regions independently of the extent of transcriptomic alterations, potentially reflecting shifts in the proportion of neurons to non-neuronal/glial cells, modifications in synaptic plasticity, or changes

99 in cell identity in response to prior reproductive experiences. Notably, the expression of neuronal
100 markers was found to be downregulated in brain regions displaying the most DEGs (**Fig. 1c**).
101 Furthermore, a significant inverse correlation between reduced neuronal marker expression and
102 the number of DEGs across all brain regions implicated changes in neuronal populations that may
103 underlie the observed transcriptional responses (**Fig. 1d**); note that this relationship was not
104 observed for other cell-types (**Extended Data 1b-f**). These findings nicely align with human
105 neuroimaging studies, which have reported reduced gray matter in mothers even years after birth,
106 a phenomenon that has been proposed to refine maternal neural circuits to optimize caregiving
107 behavior[1,2,4,19].
108
109 Based on these findings, we hypothesized that such shared neuronal marker alterations may
110 indicate common upstream mechanisms driving regional-specific transcriptional responses. To test
111 this, we first compared DEGs across brain regions to identify common gene sets that were altered
112 by parity status, which led to the observation that the greatest extent of overlap occurs in those
113 regions displaying the highest levels of transcriptional sensitivity (**Fig. 1e**). Based on these
114 analyses, we then grouped the 11 brain regions according to the number of DEGs, the degree of
115 overlap with other regions, and significant fold changes in neuronal marker expression, based on
116 the premise that these regions may be co-regulated to elicit convergent transcriptional responses
117 to parity (referred to as "high sensitivity" regions: dHF, nucleus accumbens (NAc), medial preoptic
118 area (mPOA), locus coeruleus (LC), ventral hippocampus (vHF)). Brain regions lacking these
119 criteria were classified as "low sensitivity" regions (dorsal raphe nucleus (DRN), paraventricular
120 nucleus of the hypothalamus (PVN), basolateral amygdala (BLA), ventral tegmental area (VTA),
121 olfactory bulb (OB), mPFC). Next, we explored the predicted upstream regulators of overlapping
122 DEGs in "High" versus "Low" sensitivity brain regions, which revealed several upstream

123 regulators that were grouped into common molecular classes, including hormones,
124 neurotransmitter/neurotrophin signaling molecules, transcriptional regulators, and others (**Fig. 1f**).
125 While both High and Low sensitivity regions were found to share upstream regulators within these
126 molecular classes, High sensitivity regions displayed greater enrichment for estrogen,
127 progesterone, testosterone, dopamine, and other ligands with similar receptor affinity or structural
128 homology. In contrast, regulators that were classified within the lipid category were uniquely
129 associated with Low sensitivity regions.
130
131 To further explore the regulatory networks that distinguish High versus Low sensitivity regions,
132 we performed weighted gene co-expression network analysis (WGCNA) across all 11 brain
133 regions[20], resulting in nine co-expression modules (**Fig. 1g-j**). Module-trait correlations, in which
134 the trait refers to a combination of group (NP *vs.* PP) and regional sensitivity (High *vs.* Low),
135 identified significant correlations between High sensitivity regions in PP females and the brown,
136 green, yellow, and magenta modules (**Fig. 1g;** henceforth labeled 'parity-sensitive modules'). We
137 then examined enrichment of DEGs within each module, with an extended focus on the parity-
138 sensitive modules. Consistent with our module-trait correlational analysis, parity-sensitive
139 modules displayed significant enrichment for DEGs from dHF (**Fig. 1h;** Fisher's exact tests:
140 brown, $p < 10^{-16}$; green, yellow, $p < 10^{-6}$), NAc (brown, green, $p < 10^{-3}$; magenta, $p < 0.01$; yellow,
141 $p < 0.05$), mPOA (green, $p < 0.05$; magenta, $p < 0.01$), LC (magenta, $p < 0.05$), and vHpc (magenta,
142 $p < 0.05$; yellow, $p < 0.01$). Functional annotation analysis of the genes from these modules
143 highlighted their significant enrichment in signaling pathways related to neuromodulators, such as
144 estrogen (yellow, brown) and dopamine (green, magenta), in agreement with our upstream
145 regulator analyses (**Fig. 1i, Extended Data 1k-l**). In contrast, Low sensitivity regions were

146 significantly associated with the black module, which was enriched for genes associated with RNA
147 and macromolecule processing pathways (**Fig. 1g, 1i**).
148
149 Building on these transcriptomic findings, we next investigated whether parity leads to sustained
150 functional alterations in PP females. To evaluate the extent of such persistence, we performed
151 behavioral assessments at 140 dpp, ~16-weeks after pup weaning. Behavioral tasks were selected
152 to specifically assess functions associated with brain regions displaying the most robust
153 transcriptional changes, including maternal behavior, learning, and memory. To assess maternal
154 behavior, we tested pup retrieval in the home cage by placing two donor pups in opposite corners
155 away from the nest. PP dams were observed to retrieve pups with significantly reduced latency as
156 compared to NP females (**Fig. 1j**), which is consistent with previous findings, though at a more
157 extended timepoint in our studies[21]. Next, to investigate the functional impact of dHF
158 transcriptional changes, we utilized a contextual fear conditioning paradigm. Female mice were
159 habituated to the training context before receiving five shocks (2-seconds each, 0.7 mA) with 90-
160 second intertrial intervals. Both NP and PP females demonstrated significant training acquisition,
161 as indicated by increased freezing compared to no-shock controls (**Fig. 1k**). Notably, PP females
162 exhibited enhanced acquisition, with significantly increased freezing observed by the third shock,
163 while NP females only displayed significant freezing at the fifth shock (**Fig. 1k**). During the
164 context test conducted 24-hours later, both groups demonstrated recall, with PP females showing
165 higher freezing responses than NP animals (**Fig. 1l**). Given the involvement of these brain regions
166 in anxiety- and depressive-like behaviors, we also assessed affective phenotypes using the open
167 field, light-dark box, and forced swim tests, however, no significant differences were observed
168 (**Extended Data 2a-h**). These results suggested that the transcriptional changes observed in parity-
169 sensitive brain regions may promote maternal and dHF-related behavioral outcomes, as has been

170 reported previously[7,10,12,14,22–28]. To account for the potential influence of estrous cycling on
171 behavioral changes, vaginal swabs were collected immediately following testing, and behavioral
172 analyses were stratified by estrous stage. No significant effects of estrous stage were observed
173 (**Extended Data 2i-n**), supporting parity status as the primary driver of the observed behavioral
174 differences.
175
176 ***Pregnancy and postpartum experiences promote persistent maternal neuroplasticity***
177 Since our paradigm comparing NP *vs.* PP females could not distinguish between the discrete
178 reproductive event(s) that may be responsible for the sustained transcriptional alterations observed,
179 we next sought to isolate those key events throughout the female reproductive window. To do so,
180 we compared females that were successfully bred to males but did not become pregnant (Mating
181 Only), females that experienced pregnancy and parturition but did not transition to postpartum due
182 to pup removal on the day of birth (Pregnancy Only), and virgin females exposed to 21-days of
183 donor pup interactions (Pup Sensitized). These groups were analyzed in parallel with age-matched
184 NP and PP females to delineate the contributions of specific reproductive and maternal experiences
185 (**Fig. 2a**). Consistent with previous studies[29], four days of pup exposures sensitized virgin females
186 to maternal behavior, as evidenced by increased crouching over pups and decreased pup avoidance
187 by day 4 (**Extended Data 3a**). To determine the processes conferring sustained transcriptional
188 sensitivity, we focused our investigations on the dHF due to its pronounced gene expression
189 response to parity. When comparing NP *vs.* PP gene expression profiles, we observed that the
190 Pregnancy Only group most closely resembled that of the expression profile of PP females,
191 suggesting that pregnancy is a primary driver of dHF neuroplastic changes (**Fig. 2b, Extended**
192 **Data 3b**). However, the magnitude of fold changes did not match that of the PP group, indicating

193 that additional experiences, likely during postpartum, are also necessary to fully establish parity-
194 induced changes in the dHF.
195
196 While visualization of differential expression profiles in the Mating Only and Pup Sensitized
197 groups did not mimic PP changes, comparisons to NP did identify significant DEGs across all
198 groups, with the most substantial changes observed in the Pup Sensitized group, followed by the
199 Pregnancy Only, and Mating Only groups (**Extended Data 3c-e, Extended Data Table 2**).
200 Overlapping DEGs induced by discrete reproductive events significantly intersected with DEGs
201 in PP animals, suggesting that while pregnancy is the primary driver of parity-induced effects,
202 each reproductive event contributes, in part, to this process (**Extended Data 3f**). Next, we
203 overlapped DEGs from each comparison with genes from parity-sensitive modules (from **Fig. 1**).
204 Significant overlap was observed across all groups, with Pregnancy Only and Pup Sensitized
205 groups displaying the strongest enrichment, indicating that these experiences play a key role in
206 shaping persistent dHF alterations (**Fig. 2c**). Thus, despite the lack of similarity between the overall
207 expression profiles between Pup Sensitized *vs.* PP, gene expression changes induced by pup
208 interactions likely converge on similar regulatory networks, albeit through different DEGs, which
209 are critical for parity-driven transcriptional alterations. To further explore these relationships, we
210 performed threshold-free Rank-Rank Hypergeometric Overlap (RRHO) analyses[30], which
211 demonstrated transcriptional concordance across experiences, with the strongest overlap observed
212 in pregnancy (**Fig. 2d**). These findings suggest that reproductive exposures converge, or act
213 additively, to drive the full extent of brain transcriptional changes. Furthermore, comparing GO
214 term analyses of DEGs for each group revealed significant enrichment in overlapping biological
215 processes, with many related to synaptic signaling and plasticity pathways (**Fig. 2e**). Notably,
216 certain pathways were unique to the combination of reproductive exposures, including changes in

217 CREB activity, catecholamine secretion, and myelination, indicating that these regulatory
218 processes depend on multiple reproductive events to achieve full induction (**Fig. 2e**).
219
220 Given that postpartum experiences enhanced changes that were initiated during pregnancy, we
221 conducted a controlled time course study to examine these transcriptional dynamics across
222 gestational and postpartum periods in age-matched females (**Fig. 2f**). Pregnancy timepoints were
223 selected to represent the anabolic and catabolic phases of gestation, corresponding to early (7.5
224 days post-conception, dpc) and late (17.5 dpc) stages, respectively. Postpartum timepoints were
225 chosen to capture the immediate effects of hormonal withdrawal following parturition (2 dpp), as
226 well as a later stage prior to pup weaning (21 dpp). Based on the hypothesis that parity-induced
227 transcriptional alterations are progressively enhanced across reproductive stages, we first
228 compared DEGs at each timepoint (*vs.* NP) to genes from parity-sensitive modules identified
229 previously. DEGs from all comparisons significantly overlapped with the brown module (**Fig. 2g,**
230 **left; Extended Data Table 3**), suggesting that pathways enriched in this module are central to
231 dHF programming. Enrichment in the green and yellow modules was predominantly found to be
232 induced by postpartum exposures, potentially amplifying the effects of the pathways driven by the
233 brown module (**Fig. 2g, left**). To assess the regional specificity of these dynamic changes, we
234 analyzed bulk RNA-seq data from the vHpc, a region that displayed moderate sensitivity to parity
235 status (**Fig. 2g, middle; Extended Data Table 4**), along with the mPFC, which exhibited few
236 transcriptional alterations (**Fig. 2g, right; Extended Data Table 5**). These regions exhibited
237 limited overlap of DEGs with parity-sensitive module genes, further emphasizing the specificity
238 of the pathways that drive long-term adaptations in brain regions displaying heightened sensitivity
239 to parity.
240

241 To then characterize cumulative transcriptional changes that occur across reproductive stages, we
242 performed a time course analysis using the ImpulseDE2 package to detect genes displaying
243 sustained or transient expression alterations[31]. This analysis revealed a prominent set of genes that
244 displayed persistent and progressive downregulation, with more pronounced alterations during
245 postpartum (**Fig. 2h**). These genes were significantly enriched for processes related to
246 glutamatergic synapses, dopaminergic signaling, and endocrine-related pathways (**Fig. 2i**).
247 Conversely, genes with persistent upregulation were found to be enriched for pathways associated
248 with cell junction dynamics (**Fig. 2j**), which is consistent with overall prolonged changes in
249 synaptic plasticity and transmission. Additionally, we identified gene sets displaying transient
250 alterations, including downregulation of neurogenesis-related pathways, and upregulation of
251 copper ion metabolism (**Fig. 2k-l**); these data are consistent with other studies reviewed here[32,33].
252 In total, these findings highlight postpartum as a key window for reinforcing parity-induced
253 alterations.
254
255 ***Chronic maternal stress during postpartum disrupts dHF adaptations***
256 We next examined whether postpartum perturbations may disrupt pathways that reinforce parity-
257 induced alterations in dHF. As becoming a new parent represents a significant source of stress, we
258 implemented a maternal stress paradigm that robustly increases stress hormone levels and disrupts
259 key postpartum experiences, including nursing and pup interactions, from 10–20 dpp (**Fig. 3a,**
260 **Extended Data 3g**). During this period, dams were separated from their pups for 3-hours daily
261 and were provided with limited nesting materials until pup weaning (Stress PP). As litter size
262 represents a potential confounding factor, the time period selected reduces the impact of maternal
263 stress on pup mortality that can occur immediately following birth. By 10 dpp, pups were more
264 durable, as reflected by the absence of litter size differences between Control and Stress dams

265 (**Extended Data 3h**). Accordingly, no differences in postpartum weights were observed,
266 suggesting that this postpartum stress paradigm does not induce major metabolic alterations in the
267 dams (**Extended Data 3i**). To assess the extent of parity adaptations in Stress PP, we compared
268 this group to NP and Control PP animals. Principal components analysis (PCA) of dHF
269 transcriptional profiles revealed distinct clustering of NP and Control PP groups (reproducing our
270 prior analyses), while Stress PP samples were found to cluster intermediately between the two
271 groups (**Fig. 3b**). Similarly, hierarchical clustering of all DEGs resulted in intermingling of NP
272 and Stress PP samples (**Fig. 3c, Extended Data Table 6**), suggesting that postpartum stress
273 disrupts the extent of parity alterations in dHF. To determine whether genes induced by parity are
274 reversed by stress, we then compared DEGs with opposing directionality in NP *vs.* Control PP and
275 Control PP *vs.* Stress PP groups (**Fig. 3d**). Approximately 85% of genes altered by maternal stress
276 overlapped with parity-induced gene expression changes. KEGG pathway analysis of DEGs
277 revealed shared enrichment across several pathways in both comparisons, with maternal stress
278 reversing gene expression associated with long-term potentiation, dopaminergic synapses,
279 oxytocin signaling, and other processes (**Fig. 3e**).
280
281 Since our pathway analyses indicated changes in long-term potentiation, a form of neuronal
282 plasticity that is important for learning and memory behaviors[34], we further focused our behavioral
283 assessments on contextual fear conditioning. Consistent with prior results, Control PP females
284 exhibited enhanced acquisition and context recall, as demonstrated by significantly increased
285 freezing behavior compared to NP animals. In contrast, however, Stress PP females showed no
286 significant differences *vs.* NP mice (**Fig. 3f-g**). To further evaluate dHF-dependent function, we
287 next assessed behavior using the object location task. In this test, animals were initially trained by
288 allowing them to explore two identical objects, followed by one-hour removal from the arena.

289 During the test phase, one object was displaced, and the animals' ability to identify the moved
290 object was assessed. Given prior findings that adult females require 10 minutes of training for
291 reliable discrimination[35], we first used this duration to confirm that all groups could successfully
292 identify the moved object (**Extended Data 3j**). To next assess whether Control PP females exhibit
293 enhancements in this task, we reduced the training time to 5 minutes, a duration that is sufficient
294 for learning in adult males and preadolescent female mice, but not in adult females[35]. Under these
295 conditions, Control PP females retained the ability to discriminate the novel location, whereas NP
296 and Stress PP females did not, reflecting the same pattern observed in contextual fear conditioning,
297 which was not attributed to estrous stage or locomotion (**Extended Data 3k-l)**.
298
299 ***Cell-type specific transcriptional alterations reveal dopaminergic modulation underlying***
300 ***maternal dHF plasticity***
301
302 To elucidate the mechanisms underlying parity-induced dHF plasticity, we next leveraged the
303 transcriptomic and behavioral signatures shared between NP and Stress PP groups. This
304 postpartum stress paradigm resolves key windows during which disruptions to parity adaptations
305 occur, thereby providing greater temporal resolution of the mechanisms required to sustain these
306 alterations. Building on our findings, we next performed single-nuclei (sn) RNA-sequencing on
307 these three groups to identify the dHF cell-types that integrate hormone and neurotransmitter
308 signaling to drive parity-related plasticity. Following rigorous quality control assessments to
309 remove confounding sources of variation, such as mitochondrial mapping percentage, doublets,
310 and cell-type contamination **(Extended Data 4a-f)**, we retained 109,334 nuclei for downstream
311 analysis (NP = 37,070; Control PP = 35,631; Stress PP = 36,633). Cell-type annotation was
312 performed using both manual curation and label transfer from validated hippocampal datasets from
313 the Broad Institute and Allen Brain Atlas[36,37]. This resulted in 16 distinct clusters (**Fig. 4a,**

314 **Extended Data 4g-i**), including excitatory neuron subtypes (dentate gyrus, CA1, CA3, subiculum,
315 mossy cells; 43.3% of total), GABAergic neurons (GABA.1–GABA.4; 9.1% of total), neural
316 progenitors (neural stem cells, radial glia-like cells; 9.7% of total), and non-neuronal/glial
317 populations (astrocytes, oligodendrocytes, OPCs, microglia, immune cells; 37.9% of total).
318
319 Since our cell-type deconvolution analyses indicated downregulation of neuronal markers, we first
320 assessed proportional differences across major cell-types. A Monte Carlo permutation test
321 confirmed significant shifts in several populations beyond random variation, with GABA.2 and
322 GABA.4 clusters being reduced in Control PP dHF compared to both NP and Stress PP (**Fig. 4b-**
323 **c**). We next used pseudobulk aggregation and differential expression analysis to identify DEGs
324 within each annotated cluster ($p < 0.05$ and $\log FC > |1.5|$). We observed transcriptional changes
325 across both neuronal and non-neuronal subtypes, with excitatory neuron alterations predominantly
326 observed between NP *vs.* Control PP, particularly within the subiculum (**Fig. 4d**). This pattern
327 aligns nicely with enhanced contextual fear conditioning, as prior studies have implicated altered
328 dHF excitatory outputs in improved learning outcomes in dams[24]. In contrast, the most pronounced
329 neuronal changes between Control and Stress PP were observed in the GABA.2 and mossy cell
330 populations, alongside widespread DEGs across non-neuronal cell-types (**Fig. 4d**); note that
331 differential expression analysis could not be performed for the GABA.4 cluster due to insufficient
332 sample representation in multiple groups. GO term analysis of DEGs from cell-types displaying
333 proportional differences revealed significant enrichment in pathways associated with responses to
334 endogenous stimuli (GABA.2, GABA.1, GABA.3, OPC), cell proliferation (GABA.2, CA1,
335 immune cells), synaptic function (GABA.3, subiculum), and metabolic processes (Oligo.2,
336 GABA.1) across both comparisons (**Fig. 4e-f**).
337

338 Probing deeper into these altered cell-types, we focused on the GABA.2 cluster owing to shared
339 proportional and transcriptional changes observed in comparison to both NP and Stress PP groups,
340 which suggested a common mechanism limiting dHF plasticity. Marker gene analysis revealed
341 significant enrichment of dopamine receptor D1 *(Drd1)* and D2 *(Drd2)* expression within this
342 cluster compared to other cell-types (**Extended Data 4j**), aligning with our prior bioinformatic
343 analyses implicating dopaminergic regulation. To further resolve this population, we subclustered
344 the GABA.2 cells and identified distinct subpopulations expressing *Drd1* and *Drd2*, both of which
345 appeared to be altered in Control PP animals (**Fig. 4g**). In a separate cohort of mice, we validated
346 these changes using RNA fluorescence in situ hybridization (FISH) in dorsal CA1 (**Fig. 4h-i,**
347 **Extended Data 4k-l**), where dopamine receptor-expressing interneurons have been previously
348 described[38,39]. While dopaminoceptive inhibitory neurons were implicated in our data**,** we
349 examined whether such changes extend to other dopamine-sensitive neuronal populations. RNA
350 FISH in the dentate gyrus, which contains excitatory *Drd1* and *Drd2*-expressing neurons (in
351 granule and hilar mossy cells, respectively; **Extended Data 7a**), revealed significant group
352 differences, alongside expected regional variations consistent with the sparser distribution of
353 dopamine receptor-expressing neurons in CA1[40] **(Fig. 4h-i, Extended Data 4m-n).**
354
355 Since these findings established dopaminergic signaling as a potential key mediator of persistent
356 parity-induced adaptations, this prompted us to examine whether maternal stress disrupts this
357 process within its defined postpartum window. Given prior evidence that acute pup separation
358 elevates dopamine levels in NAc[41,42], we first investigated whether a similar response occurs in
359 dHF. Brain tissues were collected from 10 dpp dams at baseline, 30-minutes, and 3-hours post-
360 separation, as well as 30-minutes post-reunion (**Fig. 4j).** We observed robust increases in
361 dopamine levels in both NAc and dHF during separation, with expected regional differences

362 reflecting the strength of innervation to these regions (**Fig. 4k**). Since acute and chronic stress
363 produce different biological responses and behavioral outcomes, we next assessed the impact of
364 repeated separation stress on dopamine modulation in these brain regions. Indeed, our data
365 revealed distinct dopaminergic responses following acute *vs.* chronic separations, with repeated
366 stress leading to loss of dopamine increases observed in response to pup separation, as well as
367 elevated baseline dopamine in both dHF and NAc tissues (**Fig. 4l, Extended Data 4o**). Loss of
368 induction following chronic stress may stem from elevated baseline levels, which facilitate
369 engagement of autoreceptors and negative feedback mechanisms[43]. Similarly, increased release of
370 dopamine in dHF tissues was not observed in NP females 30-minutes following separation from a
371 littermate (**Extended Data S4p**), though this likely lacks the same salience as pup separation.
372 These findings align with our snRNA-seq data, where decreased *Drd1/2*-expressing neurons in
373 Control PP may reflect an adaptation to reduced dopamine-related transcriptional activity (Figs. 2
374 and 3). In contrast, elevated receptor expression in NP and Stress PP animals may represent a
375 compensatory response to higher basal dopamine levels, as suggested by our observations
376 following separation stress.
377
378 ***Dopamine-dependent H3 dopaminylation enrichment is altered by parity in dHF of mice and***
379 ***humans***
380
381 Together, changes in dopamine modulation and gene expression in our mouse model point to a
382 role for dopamine-dependent epigenetic mechanisms in shaping persistent transcriptional states.
383 Motivated by this, we turned to a recently characterized class of histone post-translational
384 modifications dependent on intracellular pools of biogenic monoamines, including serotonin,
385 dopamine, and histamine, termed monoaminylations[44–46]. This process involves transamidation of
386 monoamines onto the glutamine 5 residue of histone H3 (H3Q5), a site adjacent to the canonically

387 permissive lysine 4 tri-methylation (H3K4me3), by tissue transglutaminase 2 (TG2)[47].
388 Monoaminylation at H3Q5 can coexist with H3K4me3 and is responsive to physiological and
389 environmental stimuli such as stress or drugs of abuse, with downstream effects on transcriptional
390 output[44–46,48–52]. Using our previously validated H3K4me3Q5dop antibody[45], we performed
391 CUT&RUN-seq to test the involvement of H3 dopaminylation in parity transcriptional
392 adaptations; note that this signal is lost in the absence of TG2 expression (**Extended Data Fig. 5a-**
393 **c**). Following peak calling, we found that the majority of H3K4me3Q5dop peaks annotated to
394 genic loci, with the majority of these peaks occurring within 2 kB of transcriptional start sites
395 (TSS; **Extended Data 5d-g**). In all groups, we observed that gene expression varied significantly
396 across quartiles of H3K4me3Q5dop enrichment, with higher signal associated with increased gene
397 expression (**Extended Data Fig. 5h-i**).
398
399 To examine group-specific changes in H3 dopaminylation, we identified differentially enriched
400 peaks using the DiffBind pipeline[53]. Notably, the majority of differential peaks were
401 downregulated in Control PP dHF compared to both NP and Stress PP groups (**Extended Data**
402 **Fig. 5j, Extended Data Tables 7-8**), consistent with prior results suggestive of reduced dopamine
403 tone. Integrating these peaks with DEGs from the same comparisons revealed significant overlap
404 between downregulated peaks and genes decreased in Control PP (**Extended Data Fig. 5k**),
405 implicating loss of H3 dopaminylation in the downregulation of genes modulated by parity. To
406 gain more resolution, we assessed H3K4me3Q5dop enrichment specifically at the TSS of parity-
407 regulated DEGs. Again, Control PP dHF exhibited significantly reduced signal at most loci
408 compared to NP and Stress PP (**Fig. 5a–b, Extended Data Fig. 5l**). Stratifying DEGs by
409 directionality uncovered distinct transcription factors: downregulated genes were enriched for
410 canonical repressors (Mbd3, Rest, Suz12), while upregulated genes were associated with ligand-

411 responsive nuclear receptors (Esr1, Lxr, Ppara), pointing to ligand-dependent transcriptional
412 programs that may compensate for reduced H3K4me3Q5dop by engaging alternate chromatin
413 remodeling pathways (**Fig. 5c–d**).
414
415 To assess the translational relevance of these findings, we next performed transcriptomic and
416 H3K4me3Q5dop profiling in human dorsal subiculum (dSub), a subregion of the dHF that serves
417 as its primary output and was identified in our snRNA-seq analysis as the most transcriptionally
418 responsive subregion to parity. Comparing age-matched NP subjects with parous subjects who had
419 1-2 previous births (**Extended Data Table 9**), we identified robust differential gene expression
420 indicative of long-lasting effects of parity in human brain (**Fig. 5e**). These transcriptional
421 signatures showed strong concordance with those observed in our mouse model, as determined by
422 comparison to NP *vs.* Control PP dSub pseudobulk expression profiles from our snRNA-seq data,
423 particularly for downregulated genes (**Fig. 5f**), and similarly displayed enrichment in pathways
424 related to extracellular matrix remodeling and metabolism (**Extended Data Fig 6a**). Furthermore,
425 predicted upstream transcription factor ontologies were conserved across species, with both
426 upregulated and downregulated DEGs in human dSub enriched for regulators similarly identified
427 in mouse (**Fig. 5g**). We also performed H3K4me3Q5dop CUT&RUN-seq in human dSub tissues
428 to associate such persistent gene expression signatures with dopamine-dependent chromatin
429 remodeling. Similar to our mouse tissues, we observed that the majority of H3K4me3Q5dop peaks
430 occurred at genic loci (**Extended Data Fig. 6b-d**), with increasing signal corresponding to
431 increased gene expression (**Extended Data Fig. 6e-f**). Next, we performed differential binding
432 analysis comparing parous and NP subjects. Consistent with our mouse findings, parous dSub
433 exhibited a widespread reduction in dopaminylation signal that significantly corresponded with
434 our DEG analysis (**Fig. 5h-i; Extended Data Fig. 6g; Extended Data Table 10**). Pathway

435 analysis of differentially enriched peaks revealed significant enrichment for loci involved in
436 maternal behavior, behavioral fear responses, hormone regulation, and dopamine transport -
437 processes similarly implicated in our mouse model (**Fig. 5j**). These findings suggest that parity
438 induces long-lasting dopamine-dependent remodeling of epigenomic programs in a region of the
439 human dHF, mirroring mechanisms observed in rodents.
440
441 ***Chemogenetic suppression of dopamine release into dHF recapitulates key features of***
442 ***persistent parity-induced plasticity***
443
444 Together, these findings point to conserved, parity-associated remodeling of dopamine-sensitive
445 transcriptional programs in dHF. We therefore hypothesized that persistent reductions in dopamine
446 tone may engage adaptive chromatin mechanisms to support enduring transcriptional and
447 behavioral plasticity. To assess this, we chemogenetically suppressed the dopaminergic VTA
448 projection to dHF by bilaterally expressing a floxed inhibitory neuronal hM4Di-DREADD fused
449 to mCherry (*vs.* floxed mCherry controls) in the VTA, coupled with retrograde AAVs expressing
450 a tyrosine hydroxylase (TH)-dependent Cre recombinase into the dHF (**Fig. 6a**). Selection of the
451 VTA was guided by our findings that pup separation stress drives coordinated regulation in the
452 dHF and NAc, along with its established role as a key upstream modulator of dopaminergic
453 signaling in the maternal NAc[54] (also supported by our data; **Extended Data 4q**). We validated
454 this approach by confirming selective mCherry expression in TH+ neurons of the VTA, as well as
455 reduced *Fos* expression following administration of the selective DREADD agonist
456 deschloroclozapine (DCZ; **Fig. 6b, Extended Data 5a-b**.) To minimize injection-related stress in
457 this paradigm, we sought to restrict the window of chronic DCZ administrations. Since maternal
458 stress from 10–20 dpp was sufficient to disrupt parity-induced plasticity, we posited that dHF
459 dopamine suppression during this period may correspondingly be sufficient to promote neuronal

460 adaptations in virgin NP (NP-mCherry, NP-hM4Di; **Fig. 6c**). As our comparisons aimed to
461 determine if chronic dopamine reduction in virgin females can phenocopy parity-induced
462 adaptations, we administered DCZ to postpartum dams in parallel (PP-mCherry, PP-hM4Di).
463
464 After confirming that our approach effectively suppressed dHF dopamine (**Fig. 6d**) – and did not
465 induce gross metabolic changes (**Extended Data 5c**) – we assessed behavioral outcomes 1-month
466 after the final DCZ injection (49 dpp). In the pup retrieval test, NP-hM4Di females exhibited
467 significantly reduced latency to retrieve pups compared to NP-mCherry, with no differences
468 observed relative to PP dams (**Fig. 6e**). Notably, while 8/13 NP-mCherry females failed to retrieve
469 either pup, this occurred in only 1/15 NP-hM4Di animals, comparable to PP-mCherry (0/12) and
470 PP-hM4di (1/11) dams. In contextual fear conditioning, NP-hM4Di females demonstrated
471 enhanced acquisition, mirroring the heightened learning observed in PP dams (**Fig. 6f**). In the
472 context recall test, NP-hM4Di females showed no significant differences from PP dams (**Extended**
473 **Data 5d**), though subtle effects were observed, suggesting that additional neuromodulatory
474 mechanisms may interact with dopamine to modulate the consolidation and retrieval of
475 conditioned fear responses underlying maternal behavioral plasticity.
476
477 Next, we examined whether such dopamine suppression influences cellular receptor expression in
478 the dHF. Similar to Control PP, NP-hM4Di females exhibited sustained downregulation of *Drd1*
479 and *Drd2* in both CA1 and dentate gyrus (**Fig. 6g-h, Extended Data 5e-h**). Next, we conducted
480 transcriptional profiling of the dHF in virally infected groups to assess the degree to which
481 dopamine suppression mirrors parity-associated gene expression patterns. Comparing NP-
482 mCherry *vs.* PP-mCherry expression profiles from bulk RNA-seq data, we observed an
483 intermediate expression pattern in NP-hM4Di dHF tissues (**Fig. 6i, Extended Data Table 11**).

484 RRHO analysis further supported transcriptional concordance between PP-mCherry and NP-
485 hM4Di groups in comparison to NP-mCherry (**Fig. 6j**). To next assess whether the long-term
486 transcriptional effects of prior baseline dopamine suppression align with changes in parity-
487 associated transcriptional programs, we compared NP-mCherry *vs.* NP-hM4Di DEGs to
488 previously identified parity-sensitive modules. Consistent with our behavioral findings, DEGs
489 from NP-hM4Di overlapped with the brown module but not other parity-sensitive modules (**Fig.**
490 **6k**), thereby highlighting a specific mechanistic contributor to behavioral adaptations within the
491 broader transcriptional and neuromodulatory landscape shaped by parity. Functional annotation of
492 these DEGs revealed enrichment in pathways governing synaptic plasticity and responses to
493 endogenous stimuli (**Fig. 6l**), which mirrored those found to be altered in Control PP dHF.
494
495 Finally, to assess whether the effects of dopamine suppression on dHF transcription are modulated
496 in part through H3 dopaminylation, we conducted CUT&RUN-seq targeting H3K4me3Q5dop in
497 virally-infected NP tissues. Examining H3K4me3Q5dop enrichment at the TSS of both parity-
498 regulated DEGs and genes altered between NP-mCherry and NP-hM4Di groups, we observed
499 significantly reduced signal at all loci examined in NP-hM4Di tissues (**Fig. 6m; Extended Data**
500 **Fig. 7i-j**). We identified significant transcription factors predicted for downregulated DEGs
501 between NP-mCherry and NP-hM4Di (none for upregulated DEGs), overlapping with those
502 observed in parous subjects in both human dSub and our mouse model (**Fig. 6n**). Overall, these
503 data demonstrate dopaminergic modulation as a key mechanism underlying the molecular and
504 functional adaptations associated with parity in the maternal brain (**Extended Data 5k**).
505
506 **DISCUSSION**

507 Despite decades of evidence that matrescence induces long-lasting behavioral adaptations across
508 species, the mechanisms underlying these phenomena remain poorly understood. Through
509 controlled brain-wide, time-course, and cell type-specific transcriptomic analyses – paired with
510 robust behavioral outputs, we identified gene networks, reproductive events, and neuromodulatory
511 pathways that dynamically shape regional sensitivity across pregnancy and postpartum
512 experiences, thereby promoting plasticity long after these stages have ended. In particular, our
513 study identified the dHF as a key site of sustained plasticity, consistent with its established roles
514 in spatial cognition, novelty detection, and sensory integration, which may bestow parous dams
515 with heightened sensitivity to salient environmental cues relevant for resource foraging, nest
516 navigation, and offspring survival[55–58]. While not traditionally considered a maternal behavior-
517 regulating region, the dHF integrates these salient cues to shape pup retrieval responses. Consistent
518 with our findings, lesion studies corroborate hippocampal involvement in pup retrieval
519 behavior[59,60]. Moreover, hippocampal activity modulates downstream circuits via the polysynaptic
520 VTA-hippocampal loop, which projects to the NAc and ventral pallidum - key regulators of pup
521 retrieval[58,61]. Notably, recent human studies show that maternal early life stress alters hippocampal
522 responses to infant cues[62,63], supporting chronic stress as a common interferer in the normal
523 trajectory of maternal dHF neuroadaptations. Building on this, our maternal-pup separation stress
524 model revealed that dopamine dynamics are essential for maintaining long-term neural and
525 behavioral adaptations in the maternal dHF. Indeed, in the current study we established the
526 necessity and sufficiency of maintaining appropriate dopamine tone for parity-related dHF
527 plasticity, demonstrating that chronic dopamine elevation through maternal stress, and
528 chemogenetic suppression within virgin dHF, bidirectionally modulate parity-related changes at
529 transcriptional, epigenetic, behavioral, and cellular levels. Moreover, we establish conserved

530 transcriptional and epigenetic changes in the human dSub, a subregion of the dHF. Such findings
531 implicate dopamine as a key driver of long-term maternal brain remodeling, expanding upon the
532 prevailing view that maternal dopamine function is solely driven by transient surges during
533 maternal behaviors, instead revealing a concurrent downregulation of dopamine tone in critical
534 regions, such as the dHF, to modulate persistent behavioral and cellular plasticity.
535
536 While our study focused largely on dopamine, it is notable that our chemogenetic manipulations
537 recapitulated key transcriptional and behavioral outcomes of parity, albeit not to the same extent.
538 This underscores dopamine as a crucial but not exclusive driver of parity-induced adaptations.
539 Indeed, our data also implicate hormonal contributions, including estrogen, progesterone, and
540 oxytocin signaling, in shaping transcriptional programming. Consistent with this, previous studies
541 have linked parity to estradiol-driven neuronal alterations[12], while others have demonstrated that
542 blocking oxytocin signaling disrupts parity-induced spatial learning enhancements[27]. These
543 findings suggest that parity programming arises from integration of multiple neuromodulatory
544 pathways to induce long-term effects. However, given that estrogen signaling during postpartum
545 regulates oxytocin release, which in turn modulates VTA signaling, we propose that dopamine
546 adaptations serve as a key downstream mechanism within a broader network driving sustained
547 maternal neuroplasticity[64]. Together, this work demonstrates that transient neuromodulatory
548 processes during pregnancy and postpartum drive lasting maternal neuroplasticity. Importantly,
549 this fundamental shift in brain state may interact with future experience-dependent plasticity. As
550 parity is implicated in both risk and resilience to brain disorders[65], future research should account
551 for parity status as a key variable shaping differential outcomes, particularly in its interactions with
552 other risk factors. In particular, our findings highlight an interplay between parity and stress, a key

553 risk factor for brain disorder vulnerability, in shaping maternal brain outcomes. Thus, this study
554 provides novel insights into the gene networks, dynamics, and neuromodulatory pathways that
555 drive long-lasting parity-induced adaptations, while underscoring the importance of stress
556 mitigation during pregnancy and postpartum.

557 **ACKNOWLEDGEMENTS**

558 We would like to thank members of the Maze lab for their helpful discussion on this study, and
559 members of the Nestler, Russo, and Kenny labs at the Icahn School of Medicine at Mount Sinai
560 for providing materials and/or access to behavioral equipment. We thank Dr. Min Chen, Winnie
561 Chen, Emma Andraka, and Rasika Iyer for experimental assistance. This work was partially
562 supported by grants from the National Institutes of Health: R01 MH116900 (I.M.), F32 MH126534
563 (J.C.C.), F31 NS132558 (A.M.C.), F99 NS139541 (A.M.C.), as well as funds from the Brain and
564 Behavior Research Foundation (J.C.C.), and the Howard Hughes Medical Institute (I.M.). All
565 schematics were created with Biorender.com.

566 **DECLARATION OF INTEREST**
567
568 The authors declare no competing interests.
569
570
571 **AUTHOR CONTRIBUTIONS**
572
573 J.C.C. and I.M. conceived of the study, designed the experiments, and interpreted the data. J.C.C.,
574 G.D.S., A.M.C., and S.D. performed behavioral experiments. J.C.C., G.D.S., A.M.C., and S.D.
575 performed surgeries. J.C.C., G.D.S., and C.Z. performed estrous cycle analyses. J.C.C., G.D.S.,
576 and S.D. conducted immunofluorescence and RNAscope analyses. J.C.C., G.D.S., and B.H.W.
577 performed molecular experiments. J.C.C. and E.A.B. performed single-cell sequencing

experiments. J.C.C., G.D.S., E.W. and B.H.W. performed bioinformatic analyses. N.M. and G.T. provided human tissues. J.C.C. and I.M. wrote the manuscript.

COMPETING INTERESTS

The authors declare no competing interests.

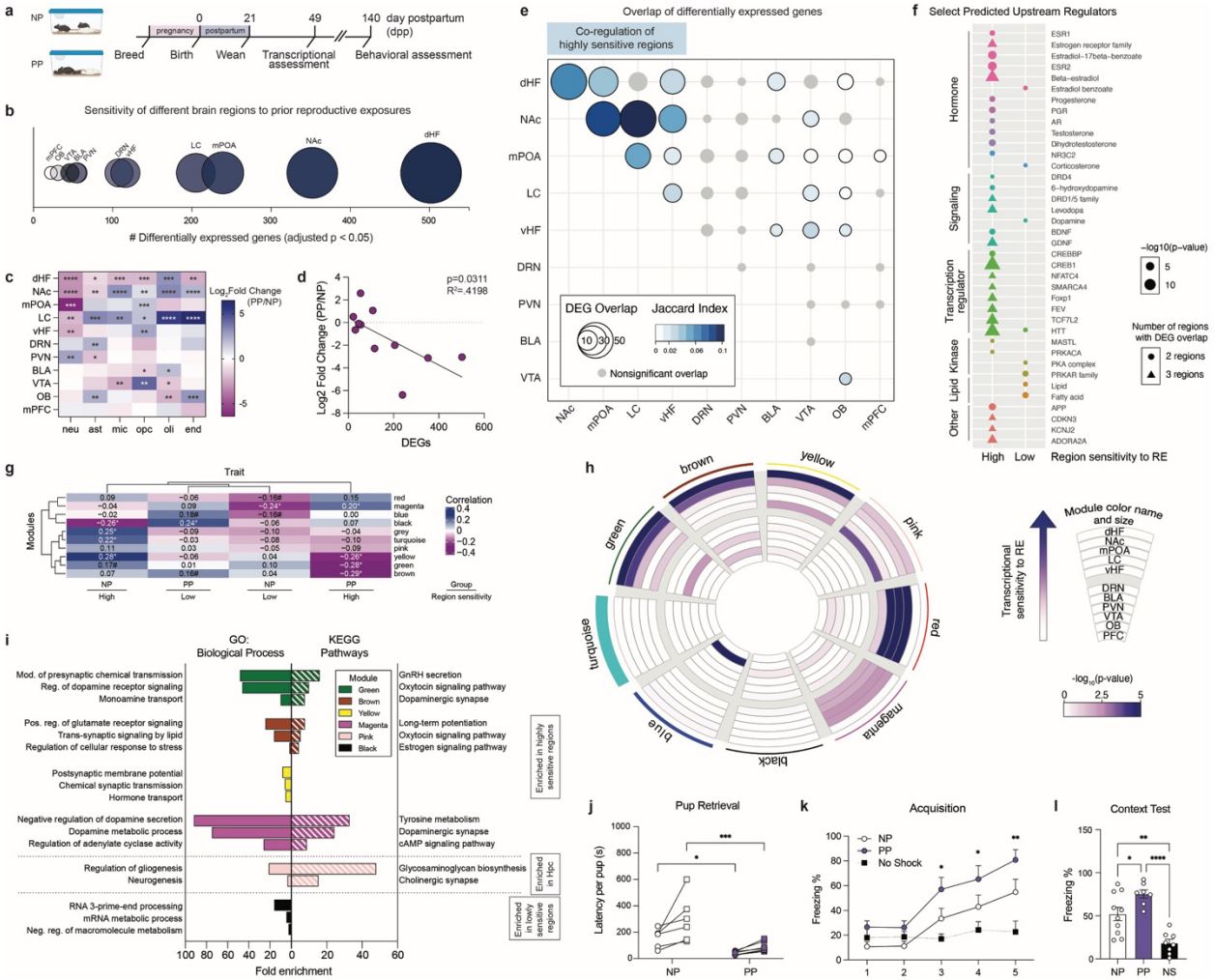

Figure 1. Pregnancy and postpartum states promote lasting transcriptional and behavioral adaptations in the maternal brain. a) Experimental timeline comparing primiparous (PP) *vs.* age-matched nulliparous (NP) female mice 1-month after offspring weaning (day postpartum, 49 dpp), and behavioral outcomes at 140 dpp. **b)** Differentially expressed genes (DEGs) per brain region. Bubble size represents total number of NP *vs.* PP DEGs (adj. $p < 0.05$). **c)** Cell-type deconvolution of bulk RNA-seq data (NP *vs.* PP normalized surrogate proportion variables, Student's t-test with multiple comparisons correction; *FDR < 0.05, **FDR < 0.01, ***FDR < 0.001, ****FDR < 0.0001). **d)** Downregulation of neuron proportion significantly correlated with number of DEGs per brain region ($R^2 = 0.4198$, $p = 0.0311$). **e)** Overlap of DEGs across brain regions ($p < 0.05$; gray indicates nonsignificant overlap). **f)** Select predicted upstream regulators of overlapping DEGs across regions with high (dHF, NAc, mPOA, LC, vHF) *vs.* low (DRN, PVN, BLA, VTA, OB, mPFC) sensitivity to parity. **g)** Trait heatmap correlating gene co-expression modules (arbitrary color names, identified by weighted gene correlation network analysis) with group x brain region classification (*$p < 0.05$, #$p < 0.1$). **h)** Circos plot for gene co-expression modules, with the size and arbitrary color name of each module indicated by the arc thickness along the perimeter. Enrichment for DEGs per brain region for each module is indicated by the inner rings, with color indicating significance of overlap. **i)** Select GO Biological Processes and KEGG Pathways significantly enriched from gene co-expression modules (FDR < 0.05). **j)** PP

605 dams retrieved both pups significantly faster compared to NP females at 140 dpp (two-way
606 rmANOVA, main effect of group ($F(1,11) = 14.47$, $p = 0.0029$), main effect of pup number
607 ($F(1,11) = 11.36$, $p = 0.0062$)), with significantly reduced latency for retrieval of pup 1 (Holm-
608 Šídák's multiple comparisons test, $t(22) = 2.301$, *adj. $p = 0.0312$) and pup 2 (Holm-
609 Šídák's multiple comparisons test, $t(22) = 4.098$, ***adj. $p = 0.0009$). N = 6-7 animals/group. **k)**
610 PP dams exhibited increased freezing behavior during the acquisition phase of contextual fear
611 conditioning (two-way rmANOVA, main effect of group ($F(2,21) = 4.259$, $p = 0.028$), main effect
612 of preshock ($F(2.827, 59.36) = 26.59$, $p < 0.0001$), interaction ($F(8,84) = 5.091$, $p < 0.0001$)),
613 compared to no shock controls (Dunnett's multiple comparisons test, *$p \leq 0.05$, **$p < 0.01$). **l)**
614 During the context recall test, PP dams froze significantly more compared to NP (one-way
615 ANOVA, $F(2,22) = 18.72$, $p < 0.0001$; Tukey's multiple comparisons test, $t(22) = 3.640$, *$p =$
616 0.044), with both groups demonstrating contextual learning compared to no shock controls (PP vs.
617 NS, $t(22) = 8.541$, ****$p < 0.0001$; NP vs. NS, $t(22) = 5.538$, **$p = 0.0021$). N = 7-10
618 animals/group. Error bars represent mean ± SEM.
619

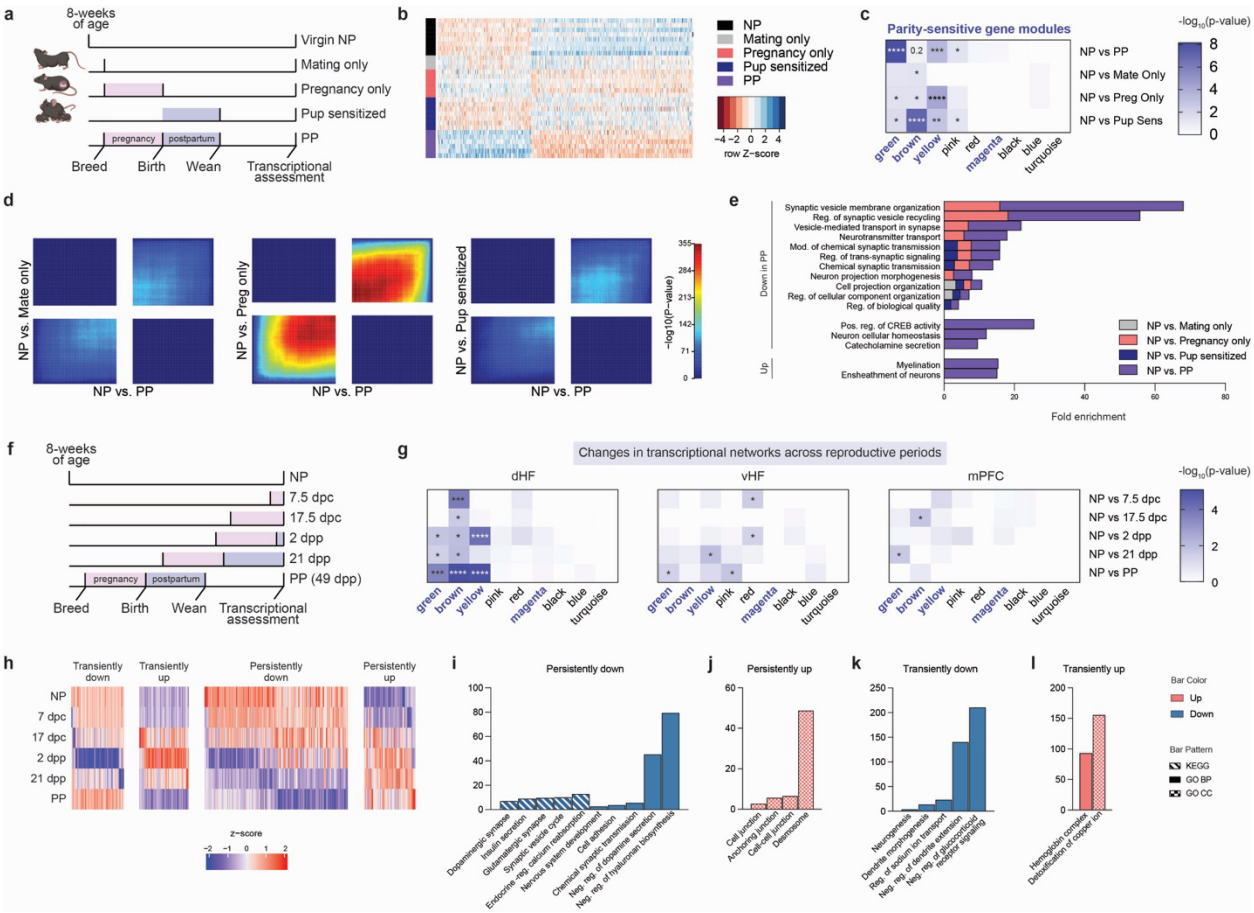

Figure 2. Parity adaptations in the dHF transcriptome integrate pregnancy and postpartum experiences. a) Experimental design to examine the contribution of discrete female reproductive events. **b)** Heatmap of differential expression profiles of top 500 genes, by ascending p-values, between NP *vs.* PP (N=3-7/group). **c)** Overlap of DEGs (*vs.* NP, adj. $p < 0.05$) for each gene co-expression module, with color representing extent of significance (*$p < 0.05$, **$p < 0.01$, ***$p < 0.001$, ****$p < 0.0001$). High parity sensitivity modules are indicated in bold. **d)** Threshold-free comparison of indicated comparisons by rank-rank hypergeometric overlap. Pixels represent the overlap of differential expression profiles indicated, with color representing extent of significance. The lower left and upper right quadrants represent concordant gene regulation. **e)** Shared changes in biological processes (identified through GO term analysis) observed following individual reproductive exposures with PP, along with processes exclusive to the combined experiences in PP (FDR < 0.05). **f)** Experimental design to examine the trajectory of PP dHF gene expression changes across pregnancy and postpartum periods (dpc: days post-conception; dpp: days postpartum). **g)** Enrichment of DEGs (*vs.* NP, adj. $p < 0.05$) with parity-sensitive gene co-expression modules across reproductive time points, examining extent of significant overlap in brain regions exhibiting high (left, dHF), moderate (middle, vHF), and low (right, mPFC) transcriptional sensitivity to parity status (*$p < 0.05$, **$p < 0.01$, ***$p < 0.001$, ****$p < 0.0001$). N=6/group. **h)** Impulse time course analysis of dHF gene expression identified patterns of transient *vs.* persistent up- and downregulation across pregnancy and postpartum (FDR < 0.05). **i-l)** Select GO terms and KEGG pathways significantly enriched for dHF genes exhibiting patterns of **(i)**

642 persistent downregulation, **(j)** persistent upregulation, **(k)** transient downregulation, and **(l)**
643 transient upregulation across reproductive stages (FDR < 0.05).
644

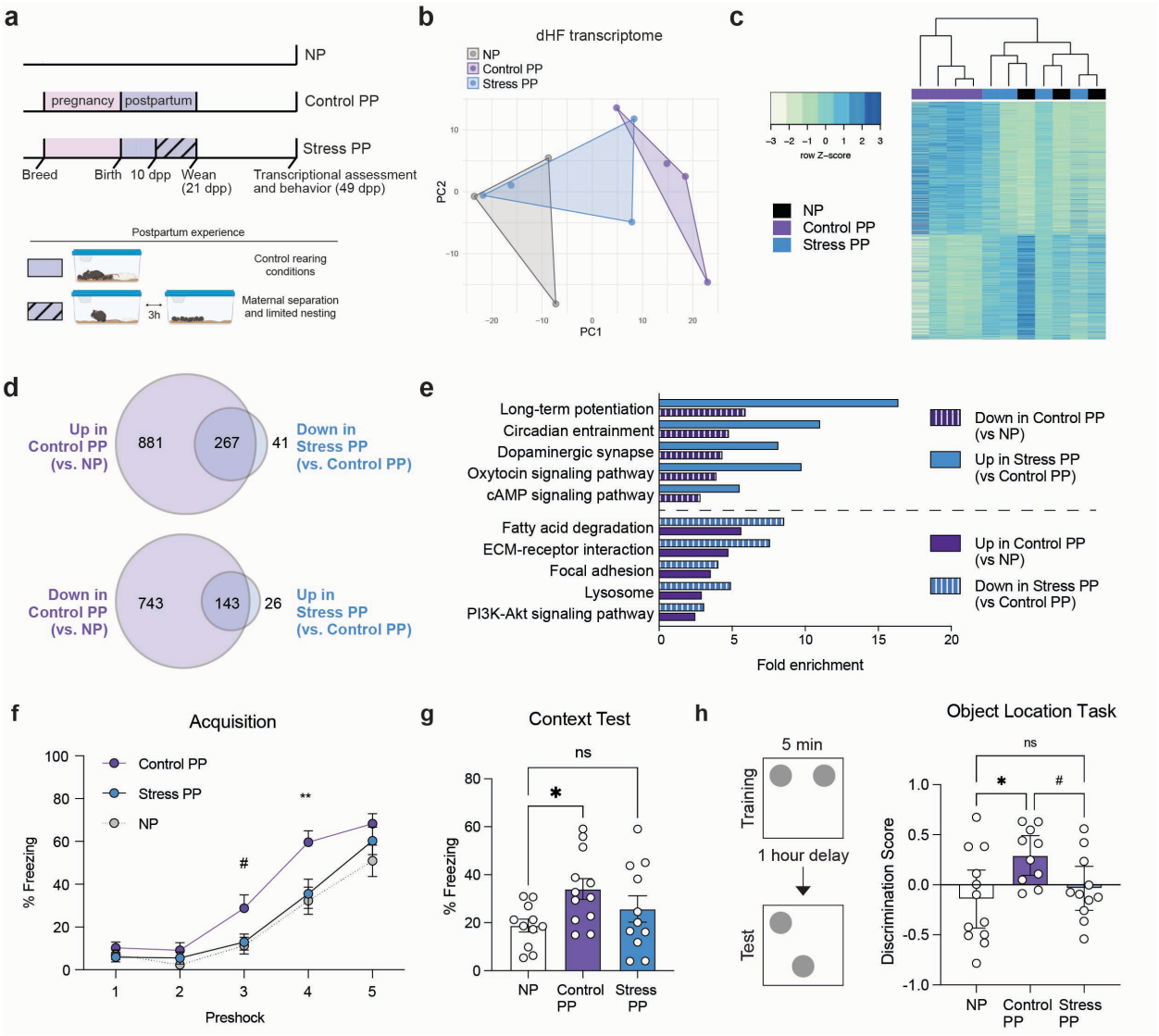

Figure 3. Postpartum stress disrupts long-term maternal dHF adaptations. a) Postpartum stress paradigm, wherein dams were provided with limited nesting and subjected to pup separation 3 hours daily between 10-20 dpp, followed by behavioral and transcriptomic assessments at 49 dpp. **b)** Principal components analysis of dHF transcriptomes, and **c)** heatmap of all significant DEGs (adj. $p < 0.05$) with hierarchical clustering. **d)** Venn Diagrams showing ~20% DEGs altered in Control PP (*vs.* NP) are significantly disrupted by postpartum stress (adj. $p < 0.05$). **e)** Parity-dependent enrichment in select KEGG pathways are significantly reversed in Stress PP (FDR < 0.05). **f)** Control PP dams froze more during the acquisition phase of contextual fear conditioning (two-way rmANOVA, main effect of group ($F(2,31) = 4.662$, $p = 0.017$), main effect of preshock ($F(3.024,93.75) = 129.8$, $p < 0.0001$), interaction ($F(8,124) = 2.406$, $p = 0.091$)), compared to NP and Stress PP (Tukey's multiple comparisons test, #$p \leq 0.1$, *$p < 0.05$, **$p < 0.01$). **g)** During the context recall test, NP froze significantly less than Control PP (one-way ANOVA, $F(2,31) = 3.151$, $p = 0.05$; Tukey's multiple comparisons test, $t(31) = 3.54$, *$p = 0.0456$), but not Stress PP (ns, $p > 0.05$). N = 11-12 animals/group. **h)** Control PP, but not Stress PP, dams spent more time investigating the moved object in the object location task compared to NP (one way ANOVA,

$F(2,30) = 4.045$, $p = 2.0278$; Holm-Šídák's multiple comparisons test: NP vs. Control PP, $t(30) = 2.764$, *adj. $p = 0.0288$; Control PP vs. Stress PP, $t(30) = 2.046$, #adj. $p < 0.1$) N=10-12 animals/group. Error bars represent mean ± SEM.

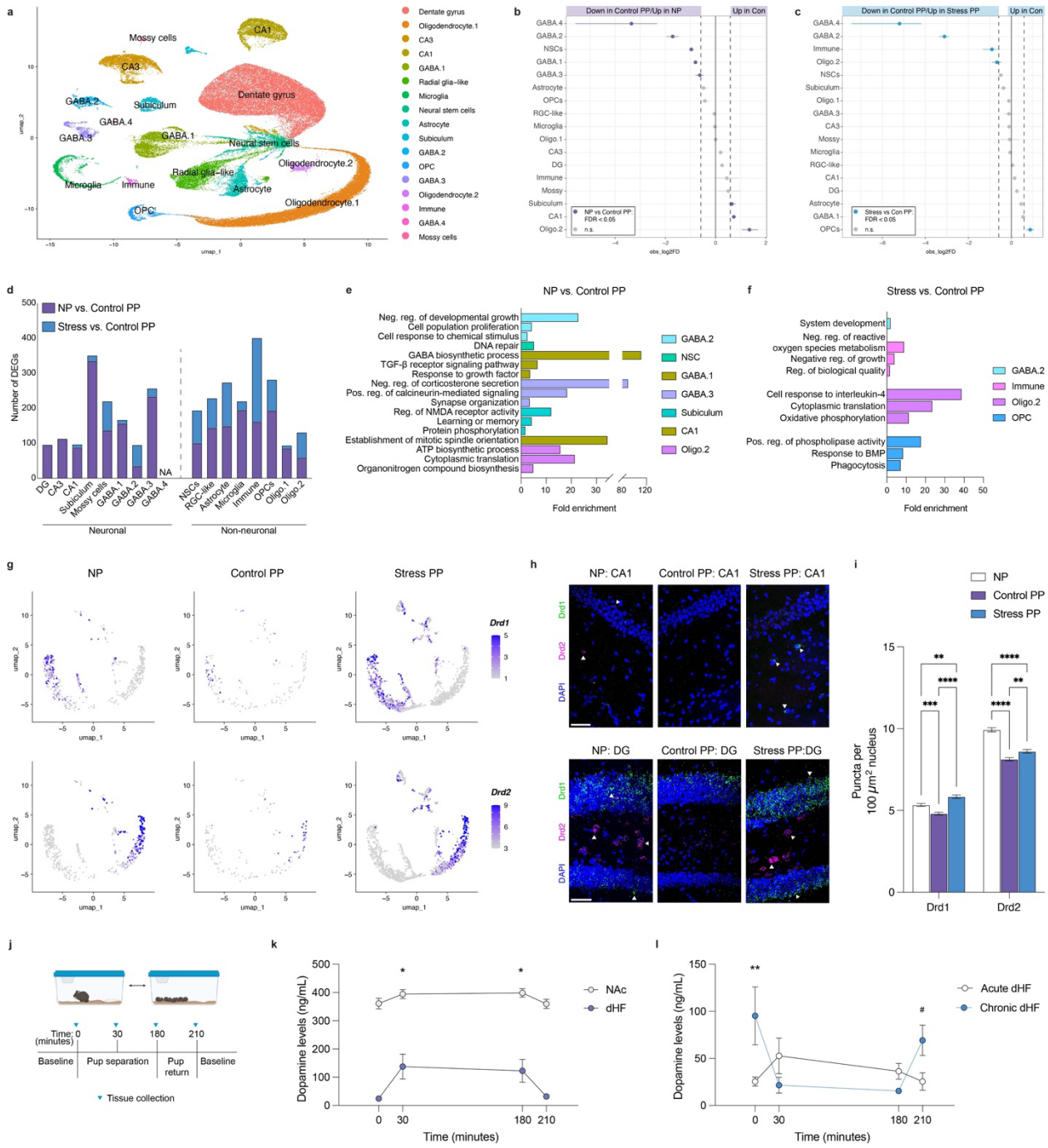

Figure 4. Parity-driven dHF plasticity is suppressed by elevated dopamine signaling. a) UMAP representation of cell clusters (109,334 total cells) from dHF tissues, colored by major cell types (N = 6 NP, 4 Control PP, 5 Stress PP). **b, c)** Point range plots depicting significant changes in proportions of major cell-type clusters between **(b)** NP vs. Control PP, and **(c)** Stress PP vs. Control PP (FDR < 0.05 and $|\log_2\text{Differerence}| > \log_2(1.5)$). **d)** Number of DEGs observed for each major cell-type following pseudobulk analysis ($p < 0.05$ and $|\log_2(\text{Fold Change})| > \log_2(1.5)$). **e, f)** GO term analyses (Biological Process) for DEGs identified in cell clusters with significant proportional differences between **(e)** NP vs. Control PP, and **(f)** Stress vs. Control PP (FDR <

676 0.05). **g)** Subclustering of GABA.2 neuronal population revealed reductions in *Drd1* (top) and
677 *Drd2* (bottom) expression in Control PP. **h)** Representative images of RNAScope for *Drd1* and
678 *Drd2* mRNAs in dorsal CA1 (top) and dentate gyrus (DG, bottom). Scale bars, 50 μm. **i)**
679 Quantification of *Drd1* and *Drd2* mRNA puncta in CA1 and DG nuclei (two-way ANOVA, main
680 effect of group ($F(2,82142) = 65.81$, $p < 0.0001$), main effect of gene ($F(1,82142) = 1771$, $p <$
681 0.0001), interaction ($F(2,82142) = 39.99$, $p < 0.0001$); Tukey's multiple comparisons test, **p <
682 0.01, ***p < 0.001, ****p < 0.0001). N = 5 animals/group. **j)** Experimental design of pup
683 separation test to examine changes in brain tissue dopamine levels. **k)** Pup separation significantly
684 increases dopamine levels from baseline in dHF and NAc tissues (two-way ANOVA, main effect
685 of time ($F(3,52) = 4.287$, $p = 0.0089$), main effect of brain region ($F(1,52) = 225.7$, $p < 0.0001$;
686 interaction ($F3,52) = 1.086$, $p = 0.3717$), with significant increases in dHF dopamine levels
687 (Dunnett's multiple comparisons test, *p < 0.05, **p < 0.01). N = 5-9 animals/time point. **l)**
688 Chronic pup separations increases baseline dHF dopamine concentrations (two-way ANOVA,
689 interaction ($F(3,53) = 4.822$, $p = 0.0048$; group $(1, 53) = 1.876$), $p = 0.1708$, time $(3, 53) = 1.736$,
690 $p = 0.1706$; Tukey's multiple comparisons test, *p < 0.05, #p = 0.06). N = 5-12 animals/time point.
691 Error bars represent mean ± SEM.
692

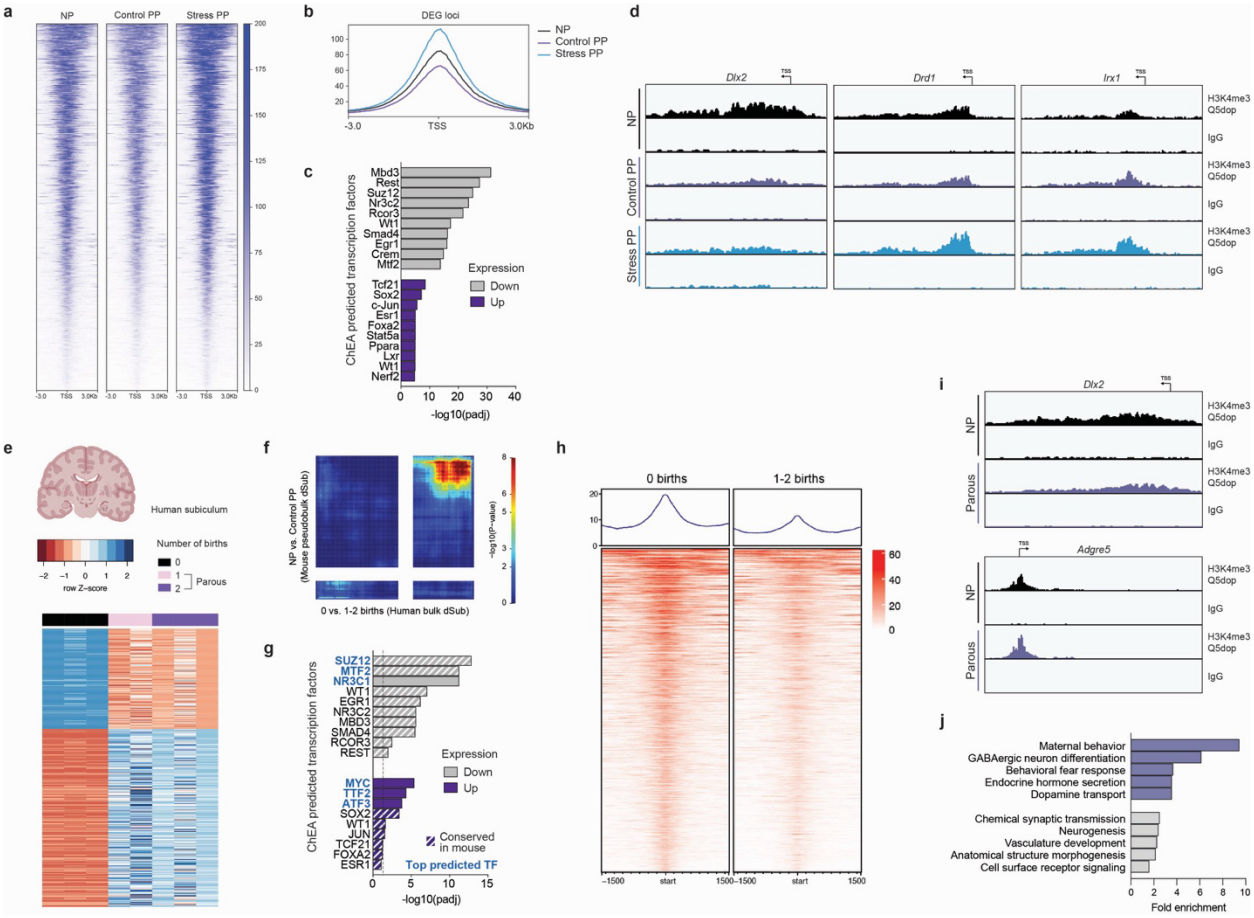

Figure 5. Parity downregulates H3 dopaminylation enrichment in dHF in both human and mice. a) Heatmaps and **(b)** profiles for H3K4me3Q5dop CUT&RUN-seq enrichment for NP vs. Control PP DEGs at TSS. Plots represent merged data from N=4 animals/group. **c)** ChEA ontology analysis identified significantly enriched transcription factors (TFs; adjusted $p < 0.05$) associated with downregulated DEGs, including a greater prevalence of repressive chromatin readers compared to those predicted for upregulated DEGs. **d)** Representative genome browser tracks for differentially enriched H3K4me3Q5dop (*vs.* IgG) peaks. Each track represents merged signal for N=4 samples/group. **e)** Heatmap of differential expression profiles of top 500 genes, by ascending p-values, from bulk RNA-seq of human dorsal subiculum (dSub) brain tissue, between NP subjects experiencing 0 births (N=3) *vs.* parous subjects previously having 1-2 births (N=5). **f)** Threshold-free comparison of human dSub RNA-seq (0 *vs.* 1-2 births) and mouse dSub pseudobulk from snRNA-seq (NP *vs.* Control PP) by rank-rank hypergeometric overlap. Pixels represent the overlap of differential expression profiles indicated, with color representing extent of significance. The lower left and upper right quadrants represent concordant gene regulation. **g)** ChEA ontology analysis showing the top three significantly enriched TFs (blue font; adjusted $p < 0.05$) associated with downregulated and upregulated DEGs from human dSub RNA-seq data. Additional TFs conserved between human and mouse analyses are indicated by white stripes. The dotted line indicates the threshold of 1.3. **h)** Heatmaps and profiles for H3K4me3Q5dop CUT&RUN-seq enrichment for human dSub, comparing subjects with 0 *vs.* 1-2 births at differential loci ($p < 0.05$, $\log_2$FoldChange $\geq |0.1|$). Plots represent merged data from 3 NP and 5 parous subjects. **i)** Representative genome browser tracks for differentially enriched H3K4me3Q5dop (*vs.* IgG) peaks

716 from human dSub. Each track represents merged signal for N=3-5 samples/group. **j)** GO ontology
717 analysis of differential H3K4me3Q5dop loci identified top significantly enriched pathways (gray
718 bars; ranked by adjusted *p*) related to synaptic signaling, neurogenesis, and vasculature
719 development. Additional significant pathways linked to maternal behavior, fear response, and
720 dopamine transport are shown in purple.

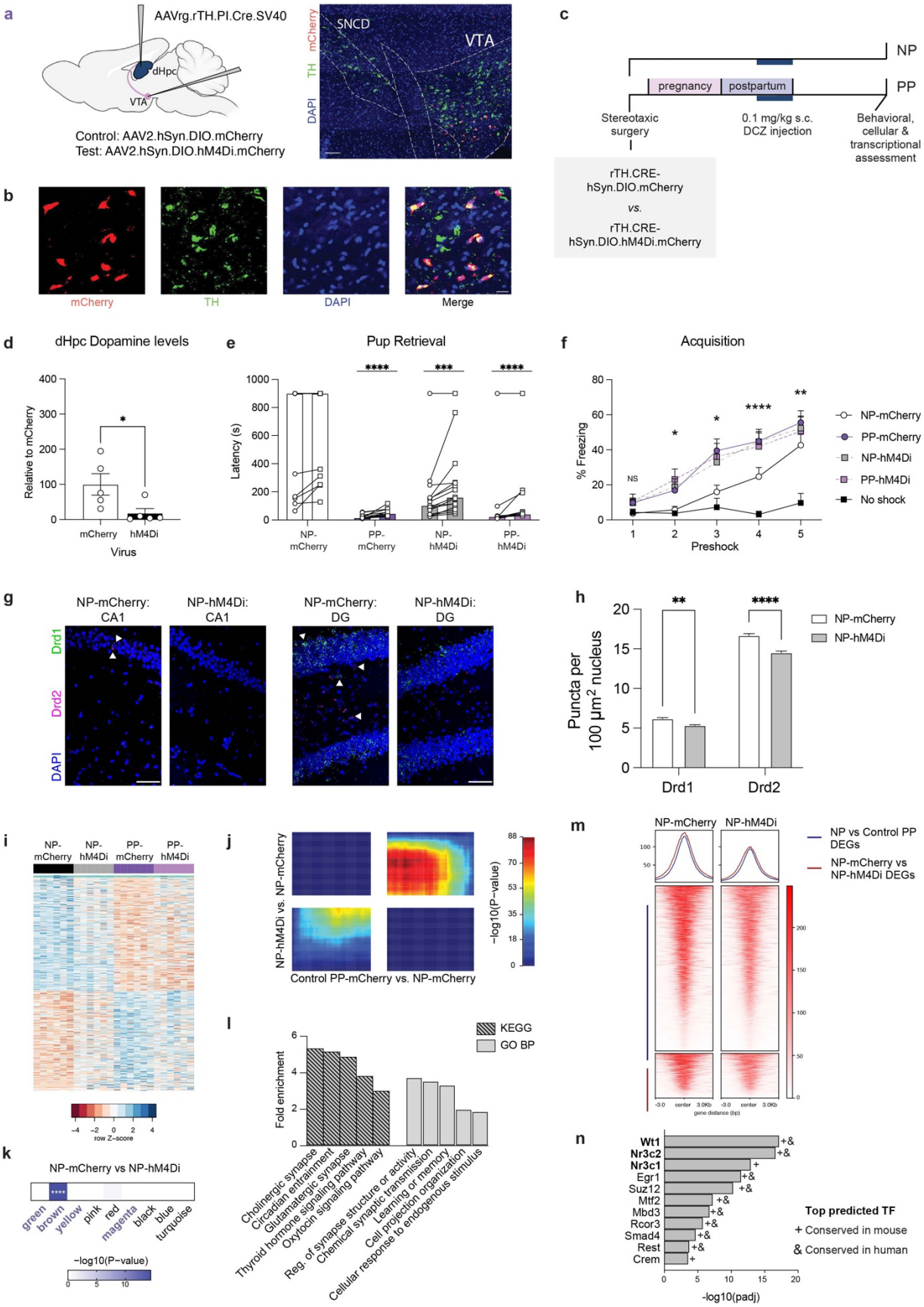
a
AAVrg.rTH.PI.Cre.SV40
dHpc
VTA
Control: AAV2.hSyn.DIO.mCherry
Test: AAV2.hSyn.DIO.hM4Di.mCherry
mCherry
TH
DAPI
SNCD
VTA
b
mCherry
TH
DAPI
Merge
c
NP
PP
pregnancy
postpartum
Stereotaxic surgery
0.1 mg/kg s.c. DCZ injection
Behavioral, cellular & transcriptional assessment
rTH.CRE-hSyn.DIO.mCherry
vs.
rTH.CRE-hSyn.DIO.hM4Di.mCherry
d
dHpc Dopamine levels
Relative to mCherry
mCherry
hM4Di
Virus
e
Pup Retrieval
Latency (s)
NP-mCherry
PP-mCherry
NP-hM4Di
PP-hM4Di
f
Acquisition
% Freezing
Preshock
NP-mCherry
PP-mCherry
NP-hM4Di
PP-hM4Di
No shock
g
NP-mCherry: CA1
NP-hM4Di: CA1
NP-mCherry: DG
NP-hM4Di: DG
Drd1
Drd2
DAPI
h
Puncta per 100 µm² nucleus
Drd1
Drd2
NP-mCherry
NP-hM4Di
i
NP-mCherry
NP-hM4Di
PP-mCherry
PP-hM4Di
row Z-score
j
NP-mCherry vs. NP-mCherry
NP-hM4Di vs. NP-mCherry
Control PP-mCherry vs. NP-mCherry
−log10(P−value)
k
NP-mCherry vs NP-hM4Di
green
brown
yellow
pink
red
magenta
black
blue
turquoise
−log10(P−value)
l
KEGG
GO BP
Fold enrichment
Cholinergic synapse
Circadian entrainment
Glutamatergic synapse
Thyroid hormone signaling pathway
Oxytocin signaling pathway
Reg. of synapse structure or activity
Chemical synaptic transmission
Learning or memory
Cell projection organization
Cellular response to endogenous stimulus
m
NP-mCherry
NP-hM4Di
NP vs Control PP DEGs
NP-mCherry vs NP-hM4Di DEGs
gene distance (bp)
n
Wt1
Nr3c2
Nr3c1
Egr1
Suz12
Mtf2
Mbd3
Rcor3
Smad4
Rest
Crem
Top predicted TF
+ Conserved in mouse
& Conserved in human
-log10(padj)

721

722
723 **Figure 6. Chronic dopamine suppression is sufficient to mimic persistent maternal dHF**
724 **plasticity. a)** Experimental design (left) and representative image (right) of
725 AAV2.hSyn.DIO.mCherry targeting to VTA projection neurons following dHF injection of
726 retrograde (rg) Cre under control of the tyrosine hydroxylase (TH) `. Scale bar, 100 µm. **b)**
727 Representative images showing overlap of virally-induced mCherry with TH+ cells in VTA. Scale
728 bar, 20 µm. **c)** Timeline of stereotaxic surgeries and s.c. deschloroclozapine (DCZ) injections from
729 10-20 dpp in NP and PP female mice, followed by experimental assessments starting at 49 dpp. **d)**
730 Significant reduction in dHF dopamine levels following inhibition of VTA projection neurons
731 (Student's t-test:t(8) = 2.477, *p = 0.0383). N=5/group. **e)** PP-mCherry, NP-hM4Di, and PP-
732 hM4Di retrieved pups faster than NP-mCherry (two-way rmANOVA, main effect of group
733 (F(3,47) = 14.39, p < 0.0001), main effect of pup number (F(1, 47) = 18.96, p < 0.0001; Sidak's
734 multiple comparisons test, ****p < 0.0001, ***p < 0.001). N =11-15/group. Bar represents mean.
735 **f)** PP-mCherry, NP-hM4Di, and PP-hM4Di freeze more compared to no shock controls at earlier
736 phases of contextual fear acquisition, compared to NP-mCherry (two-way rmANOVA, main effect
737 of group (F(4,41) = 4.739, p = 0.0031), main effect of preshock (F(2.818,115.5) = 61.92, p <
738 0.0001), interaction (F(16,164) = 2.606, p = 0.0012; Tukey's multiple comparisons test, *p ≤ 0.05,
739 **p < 0.01, ****p < 0.0001). N = 9-12/group. Error bars represent mean ± SEM. **g)** Representative
740 images of RNAScope for *Drd1* and *Drd2* mRNAs in dorsal CA1 (top) and DG (bottom). Scale
741 bars, 50 µm. **h)** Quantification of *Drd1* and *Drd2* mRNA puncta in CA1 and DG nuclei (two-way
742 ANOVA, main effect of group (F(2,33404) = 64.43, p < 0.0001), main effect of gene (F(1,33404)
743 = 2770, p < 0.0001), interaction (F(2,33404) = 12.52, p = 0.0004); Sidak's multiple comparisons
744 test, **p < 0.01, ****p < 0.0001). N = 3 animals/group. **i)** Bulk dHF differential expression profiles
745 of top 500 genes (by ascending p-values) between NP-mCherry and PP-mCherry. N=6/group. **j)**
746 Threshold-free comparison by rank-rank hypergeometric overlap, showing concordant gene
747 regulation (bottom left and upper right quadrants) between the comparisons indicated. **k)** Overlap
748 of DEGs (NP-hM4Di vs. NP-mCherry, adj. p < 0.05) with gene co-expression modules (****p <
749 0.0001). High parity sensitivity modules are indicated in bold. **l)** Select GO terms and KEGG
750 pathways significantly enriched for NP-mCherry vs. NP-hM4Di DEGs (FDR < 0.05). **m)**
751 Heatmaps and profiles for H3K4me3Q5dop CUT&RUN-seq enrichment for NP-mCherry vs. NP-
752 hM4Di at TSS for DEGs between NP vs. Control PP (top, blue line) and NP-mCherry vs. NP-
753 hM4Di (bottom, red line). Plots represent merged data from N=4 animals/group. **n)** ChEA
754 ontology analysis of downregulated DEGs identified significantly associated TFs (adjusted p <
755 0.05), paralleling patterns observed with parity in both human and mouse datasets.
756

SUPPLEMENTARY MATERIALS

Materials and Methods
Extended Data Figs. 1 to 7
Extended Data Tables 1 to 9

763 **MATERIALS AND METHODS**
764
765 **Human subjects**

766 Brain tissue used in this study was provided by the Douglas-Bell Canada Brain Bank (DBCBB;
767 www.douglasbrainbank.ca; RRID:SCR_025991). Informed consent from next-of-kin was
768 obtained for each individual included in this study. Psychological autopsies, considered the gold
769 standard for obtaining information on deceased individuals[66,67], were conducted. Briefly, these
770 consist of a series of proxy-based, structured interviews assessing psychopathology with next-of-
771 kin and complemented by reviews of medical records, as previously described[66]. Groups were
772 matched for depression diagnosis, and were otherwise neurotypical individuals who died suddenly
773 without prolonged agonal periods and did not have evidence of axis I disorders. Groups were
774 matched for postmortem interval (PMI), tissue pH, and RNA Integrity number. Frozen histological
775 grade samples of gray and white matter were dissected from the subiculum by expert
776 neuroanatomists and stored at –80 °C. Dissections were performed on 0.5 cm-thick coronal
777 sections with the guidance of a human brain atlas[68] (see also
778 http://www.thehumanbrain.info/brain/bn_brain_atlas/brain.html). Subiculum samples were
779 obtained from sections equivalent to plate 43 of the atlas (level of lateral geniculate nucleus), by
780 dissecting through the hippocampal fissure with a slight upward angle, up to the beginning of the
781 CA1 region.

782
783 **Animals**

784 Wild-type C57BL6/J mice were purchased from Jackson Laboratories at 8-weeks old, and
785 maintained on a 12-h/12-h light/dark cycle throughout the entirety of the experiments. Mice were
786 provided with *ad libitum* access to water and food throughout the entirety of the experiments. All
787 behavioral testing occurred during the animals' light cycle. Experimenters were blind to

788 experimental group, and the order of testing was counterbalanced during behavioral experiments.
789 All animal procedures were performed in accordance with NIH guidelines and with the approval
790 of the Institutional Animal Care and Use Committee of the Icahn School of Medicine at Mount
791 Sinai.
792
793 **Breeding**
794 Adult virgin female mice were pair bred in-house with age-matched males. Males were removed
795 after a maximum of 5 days, and pregnant females were singly-housed at least 2 days before
796 parturition. Pups were counted on the day of birth (0 dpp) and weaned at 21 dpp. Only dams with
797 litters between 4-10 pups were used for all experiments. On the day of weaning, dams were group-
798 housed into cages of 3-5 mice with animals of the same experimental condition. For timed
799 breedings, copulation plugs were checked every morning within 1-hour after lights on, where
800 confirmation of a plug was designated as E0.5, signaling the immediate removal of the female to
801 her own cage with a nestlet. Virgin NP females were age-matched for each experimental cohort.
802 Mating-experienced NP females were confirmed for the presence of a copulation plug. For
803 Pregnancy Only dams, pups were removed at 0 dpp within 3 hours after lights-on to minimize
804 maternal-offspring interactions. For comparison of PP dams to pup sensitized virgin females,
805 litters were culled to 4 pups to equate litter size with the number of pups used for each sensitized
806 female. In all other experiments, litters were not culled.
807
808 **Postpartum stress paradigm**
809 Stress PP females were subjected to limited nesting and maternal separation from 10-20 dpp, as
810 previously described[69–71]. On each day of separation, the entire litter was removed to a clean cage
811 with Sani-Chip bedding for 3-4 hours. Separations occurred during the light cycle, and the timing

812 varied each day to minimize predictability and acclimatization. EnviroDri nesting material was
813 depleted to 1/3 of control cages during the days of separation. Following pup weaning on 21 dpp,
814 the nesting material was restored to normal levels, and dams were group-housed into cages of 3-5
815 with animals of the same experimental condition.

816

817 **Pup sensitization**

818 Pup sensitization was conducted as previously described[22,72]. On the first day of pup sensitization,
819 virgin NP females were presented with four pups (postnatal day 5) from a cage consisting of a
820 lactating donor dam and her litter. Donor pups were exchanged for satiated pups from the same
821 litter every 8-12 hours for 21 days. Donor pups were weighed daily to ensure continual weight-
822 gain throughout the experiment, and only pups that exhibited consistent weight-gain were used.
823 Behavioral observations were conducted during the first four days of sensitization. Each dam was
824 observed for 30 minutes during the light phase for the following maternal behaviors:
825 licking/grooming, crouching, and nestbuilding. During these observation periods, females were
826 closely monitored to ensure that they did not display aggressive behavior toward the donor pups.
827 On the last day of sensitization, donor pups were weaned from the cage, and sensitized females
828 were group-housed into cages of 3-5 mice with animals of the same experimental condition.

829

830 **Brain tissue collections**

831 Animals were sacrificed by rapid decapitation. Whole brains were flash frozen with cold 2-
832 methylbutane and stored at −80°C until further processing. Flash-frozen brains were sectioned at
833 −20°C using a 1 mm mouse coronal brain matrix (Stoelting Co.). Tissues enriched for the brain
834 region of interest were micropunched using a hollow needle (Ted Pella) according to the Allen
835 Brain Atlas (see **Fig. S1A**).

836
837 **Behavioral analyses**

838 All animals (18-30 weeks, depending on the time from pup weaning) were handled for 2 minutes
839 for two consecutive days prior to initial behavioral testing. Animals were habituated to the testing
840 room for 1 hour prior to each behavioral assay. All testing occurred during the light phase.

841
842 *Pup retrieval:* All animals were individually housed for 24-hours prior to testing. Following
843 habituation, 2 pups from a donor litter with a lactating dam (aged 4-6 dpp) were placed in different
844 corners opposite to the nest in the home cage. Pup-directed interactions were recorded from above
845 for 15-minutes or until both pups were successfully retrieved into the nest. Retrieval latency was
846 calculated as [time pup was first placed into the nest by animal - time first pup was placed into the
847 cage by experimenter].

848
849 *Contextual fear conditioning:* On day 1, mice were habituated for 10 minutes to the testing
850 chamber, which consisted of a square plexiglass box with a metal grid inside a sound-attenuating
851 cabinet wiped with 70% ethanol (Med Associates, VT). On day 2, following a 3-minute baseline
852 measurement, mice were trained with five 2.0-second 0.7 mA foot shocks delivered with an
853 intertrial interval of 90-seconds. Testing for conditioned fear responses (freezing) for a total of 5-
854 minutes occurred 24-hours following training. Freezing was measured using ANY-maze software
855 connected to a camera positioned above the testing chamber. Freezing is expressed as a percentage
856 of the total test time or as a percentage of the 60-seconds prior to each shock during conditioning.
857 Animals with freezing levels exceeding 40% prior to the first shock were excluded to remove
858 potential confounding effects of heightened baseline responsivity that could interfere with
859 accurately assessing conditioned fear.

860

861 *Open Field:* Mice were placed in a 16x16 square arena under dim lighting for 5 minutes. A camera
862 positioned overhead recorded the total distance and time spent in the center *vs.* periphery using
863 Ethovision software.
864
865 *Object location task:* For training, animals were allowed to freely explore two identical objects
866 placed equidistant from adjacent corners of a 16x16 cm square arena for 5 or 10 minutes, before
867 being returned to the home cage. Following a 1-hour delay, the animals were returned to the arena
868 for testing, during which time one object was moved to the opposing corner. During the test, the
869 animals were allowed to freely explore the objects for 5-minutes. A camera positioned overhead
870 recorded time spent exploring each object using Ethovision software. The discrimination score
871 was calculated as [(time spent with moved object) – (time spent with unmoved object)/[(time spent
872 with moved object) + (time spent with unmoved object)].
873
874 *Light-dark box:* Anxiety-like behavior was tested in an apparatus containing two interconnected
875 20x20 cm compartments (Omnitech Electronics Inc.). One compartment was illuminated during
876 the session ("light" side), while the other was covered by an opaque black perspex lid ("dark"
877 side). The distance, time spent, and number of crossovers in each compartment were automatically
878 recorded by Fusion software during the 10-minute test.
879
880 *Forced Swim Test:* Mice were placed in a 4 liter glass beaker with 2 liters of room temperature
881 water for 8 minutes. Each session was recorded and scored by a blinded observer. The total number
882 of seconds that mice were immobile during the last 5 minutes of the test were recorded, as
883 previously described[73].
884

885 *Observation of pup-directed behaviors in the home cage:* Confirmation of maternal behavior in
886 pup sensitized females was conducted based on prior studies[74]. Animals were observed from the
887 first to fourth day of pup sensitization, based on published work that maternal sensitization in
888 C57BL6/J females occurs following 4-days of pup exposures[29,75]. Observations occurred in the
889 light period in the first 30-minutes after pups were placed in the cage. Each animal was scored
890 every 3-minutes, with the observed behavior recorded as one or more of the following categories:
891 nestbuilding, grooming, sniffing, crouching, nursing, eating, drinking, self-grooming, no-contact.
892 PP dams were scored for the first 4-days following birth (0-3 dpp) concurrently for comparison.
893
894 **Estrous cycle testing**
895 Vaginal samples were taken on each day of behavioral testing. 15 µL of sterile PBS was gently
896 pipetted into the vagina and mounted on a glass slide. Vaginal smears were stained with crystal
897 violet dye, washed twice with water, and cover slipped with glycerol. Three 20x images per sample
898 were acquired on a light microscope. Estrous stage was determined using the pretrained network
899 of EstrousNet[76], and confirmed afterwards by a trained experimenter based on cytology of
900 nucleated, cornified, or leukocytic cells.
901
902 **Viral Transduction**
903 Mice were anesthetized with ketamine (100mg/kg) and xylazine (10 mg/kg) i.p. and positioned in
904 a stereotaxic frame (Kopf instruments). Given the widespread changes in dopamine receptor
905 expression across dHpF subregions, we did not restrict our viral manipulations to a specific
906 subregion. 2 µl of retrograde AAV.rTH.PI.Cre.SV40 (titer ≥ 7×10^{12} vg/mL, Addgene #107788-
907 AAVrg) was infused bilaterally into the dHpF at 0.2 uL/min using the following coordinates: 7°
908 angle; anterior-posterior (AP) -2.2 mm, medial-lateral (ML) ±2.0 mm, dorsal-ventral (DV) -2.0

909 mm. 1 µl of pAAV-hSyn-DIO-mCherry (titer ≥ 4×10^{12} vg/mL, Addgene #50459-AAV2) or
910 pAAV-hSyn-DIO-hM4D(Gi)-mCherry (titer ≥ 5×10^{12} vg/mL; Addgene #44362-AAV2) was
911 bilaterally infused into the VTA using the following coordinates: 7° angle; AP -3.3 mm, ML ±0.9
912 mm; DV -4.6 mm. Needles remained in place for 7 minutes following injection to minimize virus
913 diffusion. Viral validations were conducted at least 21 days post-surgery to allow for optimal viral
914 expression and recovery.
915
916 **Chemogenetic manipulation**
917 To directly manipulate dopamine signaling in dHpF, we selectively targeted the VTA-dHpF
918 projection during a window established as being critical for dopaminergic downregulation.
919 Following 7 days of recovery, surgerized female mice were randomly assigned to NP or PP groups.
920 PP females were pair bred with naïve male mice for a maximum of 5 days, and individually housed
921 prior to parturition. From 10-20 dpp, PP females were injected subcutaneously with
922 deschloroclozapine (DCZ, Tocris #7193) – to minimize off-target effects[77] - at 1ug/kg in 1%
923 DMSO or vehicle (saline). NP females were injected with DCZ concurrently. Following weaning
924 on 21 dpp, PP dams were group-housed with animals of the same experimental condition.
925 Behavioral testing occurred beginning at 28-days post-weaning (49 dpp), and brain tissues were
926 collected following contextual fear conditioning for further analyses.
927
928 **RNAscope in situ hybridization and analysis**
929 Fresh frozen brains were cut into 12-16 µm thick slices in the coronal plane with a cryostat (Leica
930 CM3050-S), mounted on charged Superfrost Plus microscope slides (Thermofisher #P36934), and
931 stored at -80°C until processing. Sections were post-fixed with 4% PFA for 1.5 hours at 4°C, and
932 permeabolized with hydrogen peroxide (10 minutes RT) and Protease III (30 minutes RT). The

933 RNAscope Multiplex Fluorescent Reagent Kit v2 (ACD Bio) was used according to
934 manufacturer's instructions to sequentially stain sections with the following probes: Drd1a (Mm-
935 Drd1a-C1, #461901) and Drd2 (Mm-Drd2-C3, #406501-C3). RNAscope probes were visualized
936 using TSA Vivid Fluorophores (Tocris) at 1:750 dilution. Sections were counterstained with DAPI
937 (ACD Bio) and mounted using ProLong Gold Antifade Mountant (Thermo). Confocal images (3
938 images per animal, 1024 × 1024 pixels) were acquired on a Zeiss LSM 780 upright microscope
939 using a 40X objective with Zen Black software, with 5x1 tiled images. Images were averaged
940 across 8 consecutive acquisitions at a bit depth of 16 bits, with 2 z-stacks acquired per image.
941 Subcellular quantification of individual puncta per 100 µm nucleus - identified by cellular
942 detection of DAPI staining - was performed for each maximum intensity projected image using
943 QuPath software (v.0.5.1)[78]. Regions of interest (CA1 and dentate gyrus) were annotated and
944 determined by superimposing images onto the Allen Brain Atlas.
945
946 **Immunofluorescence and analysis**
947 Mice were anesthetized with isoflurane and perfused with cold 1×PBS followed by 4% PFA.
948 Brains were post-fixed in 4% PFA overnight and then transferred to a 30% sucrose/PBS solution
949 for 2 days. Brains were sectioned at 40 µm thickness using a Leica CM3050-S cryostat, with serial
950 sections collected from the VTA. For each subject, 2–3 brain slices were blocked for 2 hours (0.1%
951 Triton X-100, 10% normal donkey serum), followed by overnight incubation at 4 °C with primary
952 antibodies: chicken anti-tyrosine hydroxylase (1:500, Aves Labs #TYH) and rabbit anti-Fos
953 (1:2000, Synaptic Systems #226-008). The next day, slices were incubated for 2 hours at RT with
954 fluorescent-conjugated secondary antibodies (donkey anti-chicken Alexa Fluor 488, Invitrogen
955 #A78948; donkey anti-goat Alexa Fluor 680, Invitrogen #A10043). Slices were counterstained
956 with DAPI (1:10000, Thermo Scientific #62248) and mounted with ProLong Gold Antifade

957 Mountant (Thermo Fisher #P36934). Confocal images (2-3 replicates per animal, 1024 x 1024
958 pixels) were acquired on a Zeiss LSM 780 upright microscope using a 40x objective with Zen
959 Black software. Images were averaged across 8 consecutive acquisitions at a bit depth of 16 bits.
960 Image analysis was conducted using FIJI software (NIH). The Fos and TH channels were
961 thresholded using the MaxEntropy method to define regions of interest. Following identification
962 of colocalized Fos+/TH+ signal, Fos intensity was measured and averaged from 4-6 images per
963 animal. Brightness and contast were adjusted for representative images.
964
965 **Dopamine ELISA**
966 Brain tissue dopamine levels were assessed in response to 3 hours of pup separation in the home
967 cage. Independent biological replicates were collected at each time point, with separate animals
968 used for each measurement. Brains were rapidly harvested (see Brain Tissue Collection, above) at
969 baseline (prior to pup removal, 0 min), during pup removal (30 and 180 min), and 30 min after
970 pups were returned to the home cage (210 min). For assessment of NP females, samples were
971 collected in the home cage 30-min following removal of a littermate. Equal weights of
972 micropunched brain tissues were homogenized in lysis buffer (0.01 N HCl, 1 mM EDTA, 4 mM
973 sodium metabisulfite). Tissue dopamine levels were assessed using the Dopamine (Research)
974 ELISA Kit (ALPCO Diagnostics) according to manufacturer's instruction.
975
976 **HPA axis assessment**
977 Plasma corticosterone levels were assessed in response to 3-hours of pup separation in the home
978 cage. Testing was initiated within 2-hours after lights on. Tail blood was collected prior to pup
979 removal (0 min), during pup removal (30 and 180 min), and 120 min after pups were returned to
980 the cage (300 min) from the same animals. Samples for control animals in the home cage, used to

981 account for the effects of handling-induced stress, were collected concurrently. Blood samples
982 were immediately mixed with 50 mM EDTA and centrifuged at 5000 rpm for 10 minutes. Plasma
983 was collected and stored at −80 °C until analysis. Corticosterone levels were quantified using a
984 Corticosterone ELISA kit (ENZO Life Sciences) according to manufacturer's instruction.
985
986 **Clonal *TGM2* Knockout in HeLa cells**
987 HeLa cells (ATCC, CCL-2) were cultured at 37 °C with 5% CO_2 in DMEM medium (high-glucose,
988 ThermoFisher 11965118) supplemented with 10% FBS (Sigma-Aldrich) and 500 U ml−1
989 penicillin and streptomycin. The CRISPR guide RNA targeting exon 5 of *TGM2* was purchase
990 from IDT, containing the sequence ACGCTGGGACAACAACTACG. 120 pmol of guide RNA
991 and 100 pmol of Alt-R™ S.p. Cas9 Nuclease V3 (IDT, 1081058) were premixed for 15 minutes
992 in 5 μL total (with PBS). 200k HeLa cells were washed in PBS, before resuspending in 20 μL of
993 nucleofector solution (SE Cell Line 4D-Nucleofector® X Kit S, Lonza V4XC-1032). The 5 μL
994 Cas9/sgRNA mix was added, as well as 1 μL of Alt-R Cas9 Electroporation Enhancer (IDT,
995 NC1395977), and all mixed gently. The entire mixture was transferred to a 16-well Nucleocuvette
996 strip (Lonza, PDH-2104) gently, and nucleofected using the Lonza 4D-Nucleofector® X Unit,
997 using the default settings for HeLa cells. Directly after nucleofection, 80 uL of pre-warmed culture
998 media was added to the cuvette. The entire mixture was immediately transferred to a 6 well plate
999 with 2 mL of prewarmed culture media, and incubated cultured at 37 °C with 5% CO_2 for 48 hours.
1000 Nucleofection efficiency was assessed by using a second positive control reaction with a pMax-
1001 GFP plasmid (Addgene, 177825). The pool of cells was diluted to a concentration of 1 cell per 200
1002 uL, and 100 uL aliquoted into each well of 10 96 well plates, and cultured at 37 °C with 5% CO_2.
1003 After 14 days, single-clones were identified using a light microscope. Single-clone containing
1004 wells were expanded and targeting assessed by extracting genomic DNA and performing PCR and

1005 PCR sequencing over the targeted site (Fwr: GGCTCCAGCCCCCACCATCTGCCGCAC, Rev:
1006 GCCACATAGCGCATTGAGAGTGTTGGT). PCR sequencing results were assessed using
1007 Synthego's ICE analysis. Clones which were identified as introducing premature stop codons were
1008 expanded further.
1009
1010 **Assessment of *TGM2* KO Cell Line**
1011 *Western Blot for TG2*: Briefly, HeLa cells were collected and lysed using high-salt buffer (20 mM
1012 HEPES pH 7.9, 500 mM KCl, 10 mM MgCl2, and 1 % NP-40), followed by brief pulse-sonication.
1013 100 ug of protein was run on a 4-12% Bis-Tris gel (Invitrogen, NW04122) for 45 minutes at 150V.
1014 Protein was transferred to a 0.2 µm nitrocellulose membrane using a Trans-Blot Turbo Transfer
1015 System (BioRad) following the manufacturers protocol. The membrane was blocked in 5% milk
1016 in TBS for 1 hour, and primary antibody (anti-TG2, Abcam 2386, 1:500 in 1.5% milk in TBS)
1017 overnight at 4° C. The blot was washed 3 x 15 minutes in TBS-T, and then incubated with
1018 secondary antibody (Goat anti-Mouse IgG (H+L) Cross-Adsorbed Secondary Antibody, Alexa
1019 Fluor™ 647, Invitrogen A-21235) at room temperature for 1 hour, followed by washing 3 x 15
1020 minutes in TBS-T. The blot was imaged using a BioRad ChemiDoc MP, and then the blot was
1021 stained with amido-black stain to assess total protein loading.
1022
1023 *Transamidation Activity Assay*: 100 ug of HeLa extract was diluted in low-salt buffer (20 mM
1024 HEPES pH 7.9, 150 mM KCl, 10 mM MgCl2), and 1X final transamidation assay buffer was
1025 added (25 mM Tris-HCl, pH 8, 10 mM CaCl2, 10 mM DTT, 10 mM KCl). Biotin-cadaverine
1026 (Millipore Sigma A5348) was added to a final concentration of 1 mM, and reactions incubated at
1027 30° C for 2 hours. A western blot was run as described above, using a Streptavidin-Alexa Fluor™
1028 488 Conjugate (ThermoFisher S32354) to measure incorporation of biotin-cadaverine.

1029
1030 **Statistics**

1031 Statistical analyses for behavioral and immunoassay data were conducted using Prism software
1032 (GraphPad, v.10.4.1). Data distribution was assessed for normality. Data that met assumptions of
1033 normality were analyzed using parametric tests, while non-normally distributed data were
1034 analyzed using non-parametric alternatives. For experiments involving multiple conditions, one-
1035 way or two-way ANOVAs were performed, followed by *post hoc* analyses when appropriate. For
1036 time course analyses where multiple measurements were taken from the same animal, repeated
1037 measures ANOVAs were performed. Two-tailed Student's t-tests were used for comparisons
1038 between two conditions. Behavioral data derived from manual observations and pregnancy/litter
1039 outcomes were analyzed using chi-square tests. Grubb's test (alpha = 0.05) was applied to detect
1040 outliers where necessary. Statistical significance was defined as $p \leq 0.05$.

1041
1042 **Bulk RNA-seq and analysis**

1043 *RNA isolation and library preparation:* Total mRNA was extracted from frozen brain tissues after
1044 homogenization in Trizol Reagent (Thermo Fisher) and cleaned using RNeasy Microcolumns
1045 (Qiagen) following the manufacturer's instructions. For RNA-seq library preparation, 150 ng of
1046 mRNA per sample was used with either the Illumina Stranded mRNA Prep Kit (Illumina,
1047 #20040534) or the TruSeq RNA Library Prep Kit v2 (Illumina, #RS-122-2001), according to the
1048 manufacturer's protocols. Library quality was assessed using a Qubit Fluorometer 2.0 (Thermo
1049 Fisher) and a High Sensitivity D5000 TapeStation assay (Agilent) before sequencing on a NovaSeq
1050 6000 or NovaSeq X system.

1051
1052 *Differential expression analysis:* Raw fastq files, containing an average of 20–30 million reads per
1053 sample, were processed for pseudoalignment and abundance quantification using Kallisto (v.

1054 0.46.1) against the Ensembl Mus musculus reference (v. 79)[79]. To filter lowly-expressed genes,
1055 only those with a total read count of at least 10 across all samples were retained. To account for
1056 unwanted variation among samples within each sequencing experiment that could arise from
1057 technical or biological factors unrelated to the conditions of interest (including litter size, estrous
1058 stage, day of sample collection, etc.), RUVs (v1.32.0) was applied with a negative control gene set
1059 derived from the total genes identified per sequencing experiment, after ensuring that unwanted
1060 variation did not correlate with covariates of interest, as described previously[80,81]. Differential
1061 expression analysis was performed using DESeq2 (v1.38.3)[82], with significant genes defined by
1062 an adjusted p-value < 0.05. For brain-wide transcriptome comparisons in which samples were
1063 processed across multiple sequencing runs and stemming from separate cohorts, pairwise
1064 comparisons were performed independently for each brain region. For all other experiments, where
1065 subjects came from the same cohort and were processed in a single sequencing run, all groups
1066 were analyzed together to maintain consistent normalization within the experiment. Gene
1067 expression time course analyses examining the periods before, during, and after pregnancy and
1068 postpartum were performed on normalized count data using the ImpulseDE2 package (v0.99.10)[31]
1069 for each brain region. Significant genes exhibiting transient regulation or monotonous changes in
1070 expression were identified using case-only differential expression analysis, with a Q-value
1071 threshold of 0.05.
1072
1073 *Weighted gene co-expression analysis:* To identify brain-wide gene co-expression networks,
1074 normalized count data for all brain regions were compiled and analyzed using the WGCNA
1075 package (v1.73)[20]. Co-expression networks were constructed from the 7,500 most variable genes,
1076 determined by ranking gene variance. A soft threshold power of 12 was identified with the
1077 pickSoftThreshold function to ensure scale-free network properties. Modules were identified

1078 based on dissimilarity of a signed topological overlap matrix (TOM), and named with an arbitrary
1079 color. The "gray" module encompassed genes that did not segregate into any specific module, and
1080 was therefore removed from further analyses. To assess the enrichment of differentially expressed
1081 genes (DEGs) within each brain region per module, Fisher's exact tests were performed using the
1082 fisher.test() function in R (v4.3.0). To analyze the correlation between gene modules and brain
1083 regional sensitivity to parity, brain regions were categorized into two groups based on the top five
1084 regions with significant DEG overlap. These regions were designated as "High Sensitivity"
1085 regions, while all other regions were classified as "Low Sensitivity." Pearson correlation
1086 coefficients were calculated to examine the relationship between each module and the trait
1087 (regional sensitivity × parity status), with statistical significance determined by Student's t-tests (p
1088 <0.05). Heatmaps were generated to visualize these module-trait correlations, and module-specific
1089 gene lists were exported for pathway enrichment analysis.
1090
1091 *Pathway and predicted upstream regulator analyses:* Functional annotation of DEGs was
1092 conducted using ShinyGO (v0.81)[83], with all protein-coding genes in the mm10 genome used as
1093 the background. Pathways with an FDR < 0.05 were considered significant. All significant
1094 pathways and associated statistics are provided in the Supplementary Tables. For figures, relevant
1095 pathways were selected from the top 10 or 1/3 of significant terms, ranked by FDR, to emphasize
1096 processes consistent with hypotheses informed by published literature. For GO term selection,
1097 Revigo[84] was used to reduce redundancy of overlapping GO terms when needed. Ingenuity
1098 Pathway Analysis (IPA; Qiagen, Inc., v.01-23-01) was used to predict upstream regulators for
1099 DEG lists[85]. For "High Sensitivity" and "Low Sensitivity" regions (see *WGCNA* section), DEGs
1100 shared by at least two or three brain regions were extracted, irrespective of the direction of change.
1101 The IPA software was used to identify upstream regulators associated with each DEG list, with

1102 statistical significance defined as $p < 0.05$. To investigate the mechanisms underlying parity
1103 programming of dHpF plasticity, significant upstream regulators were systematically prioritized
1104 based on one or more of the following criteria: (1) multiple molecules involved in the same
1105 signaling pathways (e.g., progesterone and its receptor, PGR); (2) structurally similar molecules
1106 that engage analogous signaling cascades (e.g., levodopa and dopamine); (3) molecules known to
1107 be influenced by reproductive exposures; (4) molecules demonstrated to play a role in hippocampal
1108 plasticity; (5) molecules identified as significant in both "High Sensitivity" and "Low Sensitivity"
1109 regulator lists; and (6) molecules with high statistical significance values. Following selection,
1110 upstream regulators were categorized into general molecular classes (e.g., "Hormone,"
1111 "Transcription Factor," "Lipid") and grouped for visualization. Data are presented as a bubble plot,
1112 with marker shape representing number of brain regions sharing DEGs and marker size
1113 corresponding to significance.
1114
1115 *Gene expression overlap analyses:* Jaccard indices were calculated for overlapping gene lists using
1116 the GeneOverlap package (v1.36.0)[86], with significance defined by $p < 0.05$. Fisher's exact tests
1117 were calculated using the base *fisher.test()* function in R (v. 4.3.0) following construction of
1118 contingency tables for each comparison. Transcriptome-wide, threshold-free gene expression
1119 overlap was visualized using Rank-Rank Hypergeometric Overlap (RRHO) heatmaps generated
1120 with the RRHO2 package (v1.0)[30]. Gene lists were ranked by signed p-values, calculated as the
1121 log10-transformed nominal p-value multiplied by the sign of the fold change, without applying
1122 differential expression thresholds.
1123
1124 *Cell-type deconvolution:* Brain cell-type proportion was estimated from normalized expression
1125 data using the BRETIGEA package (v.1.0.4)[18] with default markers. For comparisons between

1126 groups, surrogate proportion variables were normalized using the Normalize function in Prism
1127 (GraphPad, v. 10.4.1). Each sub column was normalized separately, with the smallest value set to
1128 0% and the largest value set to 100%. To calculate $\log_2$(fold change) between groups, normalized
1129 values per cell-type per group were averaged and expressed as the log2 ratio of the group means.
1130
1131 **Single nuclei RNA-seq**
1132 *Nuclei isolation and library preparation:* For each animal, 2 mm dHpF-enriched tissue
1133 micropunches were collected bilaterally from consecutive 1 mm slices from -0.80 to -2.80 mm
1134 relative to bregma for a total of 4 punches (Ted Pella). Samples were processed in batches of 4-6,
1135 with each group represented within each batch. Nuclei were isolated using a modified version of
1136 a sucrose density gradient isolation protocol[87]. Briefly, thawed tissues were placed in 1 mL of lysis
1137 buffer (0.32 M sucrose, 5 mM $CaCl_2$, 3 mM magnesium acetate, 0.1 mM EDTA, 10 mM Tris-HCl
1138 pH 8, 1 mM DTT, 0.1% Triton X-100) with 50 µL of 25 U/mL RNase inhibitor (Takara #2313B)
1139 in a dounce homogenizer (Wheaton #357538). Homogenization was performed with 20 strokes
1140 using a tight pestle. Another 1 mL of lysis buffer was added, followed by an additional 10 strokes.
1141 The resulting 2 mL homogenate was transferred to a 15 mL Open-Top Thinwall Polypropylene
1142 Tube (Beckman-Coulter #361707). The homogenizer and pestle were rinsed with 2 mL of lysis
1143 buffer, and this wash was combined with the homogenate for a total of 4 mL. The homogenate
1144 was carefully underlaid with 9 mL of sucrose solution (1.8 M sucrose, 3 mM magnesium acetate,
1145 1 mM DTT, 10 mM Tris-HCl pH 8) and ultracentrifuged at 24,000 rpm for 1 hour at 4 °C using a
1146 Sorvall™ WX+ centrifuge. After centrifugation, the supernatant and debris at the interface were
1147 gently removed. The nuclear pellet was resuspended in 1 mL of resuspension buffer (0.02% bovine
1148 serum albumin in DPBS with 25 µL of 25 U/mL RNase inhibitor) and incubated on ice for 10
1149 minutes. The suspension was passed through a 35 µm nylon mesh filter (Corning #352235) into a

1150 1.5 mL RNase/DNase-free microcentrifuge tube and centrifuged at 2600 x g for 10 minutes at 4
1151 °C. Supernatants were discarded, and nuclei were resuspended in 200 µL of resuspension buffer.
1152 A 10 µL aliquot of the nuclei suspension was stained with Trypan Blue to assess quality and
1153 concentration using a Countess 3 Automated Cell Counter. Nuclei suspensions were loaded onto
1154 a Chromium Single Cell 3′ chip (10X Genomics, v3) and processed according to the manufacturer's
1155 protocol, targeting 10,000 nuclei. Single-nuclei libraries were generated using the 10X Chromium
1156 Next GEM Single Cell 3′ v3.1 (Dual Index) protocol (CG000315 Rev A). Libraries were pooled,
1157 loaded onto a single 10B 100 Cycle Flowcell, and sequenced using an Illumina NovaSeq 6000
1158 system to generate 25-30,000 paired-end 2 × 100 bp reads.
1159
1160 *Data analysis:* FastQ files were processed with the 10X Genomics Cell Ranger pipeline (v7.1.0)
1161 to demultiplex reads, align them to the mouse genome (mm10-2020-A), remove PCR duplicates,
1162 and generate gene expression matrices. Cell Ranger filtered outputs were analyzed using Seurat
1163 v4.3.0[88], and mitochondrial RNA content per cell was calculated using the GRCm39 (mm10)
1164 genome annotation and regressed out using SCTransform normalization protocol included in the
1165 Seurat toolkit with 20 principal components (PCs) and a resolution of 0.1. To estimate ambient
1166 RNA and correct for background contamination, the SoupX (v1.6.2) package[89] was used for each
1167 sample using raw and filtered feature matrices from the Cell Ranger output. Heterotypic doublets
1168 were identified and removed using DoubletFinder (v2)[90] to ensure the integrity of singlet datasets.
1169 Filtered singlet datasets were then re-normalized and integrated using the same Seurat
1170 SCTransform v2 workflow mentioned above. Cell clusters were annotated using a combination of
1171 expert curation based on published marker genes[37,91–96], and label transfer from hippocampal
1172 reference datasets, including the Allen Brain Map and Broad Institute resources[36,37]. Clusters with
1173 contaminant cell populations expressing markers for choroid plexus (*Ttr*), ependymal (*Tmem212*),

1174 and vascular leptomeningeal cells (*Vtn, Col1a2*) were removed from the analysis[96–99].
1175 Additionally, as the sequential 2mm micropunches encompassed portions of cortical, thalamic and
1176 vHpF regions, clusters characterized by enrichment of published non-dHpF neuronal markers
1177 using Seurat's FindMarkers function (layer 5/6 cortical: *Rorb, Foxp2*[99]; ventral granule neurons:
1178 *Tox3*[93]) were also removed from the analysis. Cell cluster proportion analyses were conducted
1179 using the scProportionTest package[100], which employs a Monte Carlo permutation test to evaluate
1180 whether observed differences result from random sampling. Proportional differences between
1181 conditions were compared to a null distribution generated by resampling, and statistical
1182 significance was determined by permutation-based p-values with confidence intervals estimated
1183 via bootstrapping. Differential expression analysis was conducted using pseudobulk analysis,
1184 where gene counts were summed across all cells within each sample for each cell type cluster using
1185 the AggregateExpression() function. DESeq2 was then applied at the sample level to conduct
1186 differential expression. To explore pathways underlying cluster-specific differences across
1187 conditions, pathway analysis was conducted using ShinyGO on genes meeting the following
1188 criteria: $\log2FC > 1.5$ and $p < 0.05$.
1189
1190 **CUT&RUN-seq**
1191 *Cleavage Under Targets and Release Using Nuclease:* The procedure was adapted from
1192 established protocols[46,101]. For mouse brain tissue, two unpooled 1.5mm dHpF punches were used
1193 for each biological replicate and split across three reactions (H3K4me3Q5ser, H3K4me3, IgG).
1194 For human brain tissue, ~10mg of tissue dissected from individual frozen subiculum samples was
1195 collected from each subject, and split across the indicated antibodies. Samples were dounce
1196 homogenized in nuclear extract (NE) buffer (20mM HEPES-KOH pH 7.9, 10mM KCl, 0.5mM

1197 spermidine, 0.1% Triton-X, 20% glycerol with protease inhibitors) and passed through a 21 gauge
1198 needle 10x. Nuclei were pelleted at 1,100g for 5 min at 4 °C in a swinging-bucket rotor, passed
1199 through a 40 µM strainer (pluriSelect USA), washed again in 500 µl NE buffer and counted.
1200 BioMag Plus Concanavalin A beads (Polysciences) were prepared per reaction by washing three
1201 times with binding buffer (20 mM HEPES-KOH pH 7.9, 10 mM KCl, 1 mM $CaCl_2$, 1 mM $MnCl_2$).
1202 Beads (15 µl) were aliquoted into 1.7 ml DNA low-bind tubes (Eppendorf) containing 500 µl NE
1203 buffer and 100,000 nuclei per reaction. Samples were rotated at room temperature for 10 min, then
1204 bead-bound nuclei were washed three times with wash buffer (20 mM HEPES pH 7.5, 150 mM
1205 NaCl, 0.1% Triton X-100, 0.1% Tween-20, 0.5 mM spermidine, 0.1% BSA, and protease
1206 inhibitors), resuspended in 100 µl antibody buffer (wash buffer with 2 mM EDTA), and mixed.
1207 2 µl antibodies were added to the corresponding tubes: H3K4me3 (Active Motif, 39159),
1208 H3K4me3Q5dopaminyl (Millipore, ABE2590), or rabbit IgG (Invitrogen, 10500c). Samples were
1209 incubated overnight at 4 °C on a rotating mixer angled upward at 20 degrees. The next day, nuclei
1210 were washed twice with cold wash buffer, and incubated with 2.5 µl pAG-MNase (Epicypher, 15-
1211 1016) for 1 h at 4 °C. After four washes with cold wash buffer and one with low-salt rinse buffer
1212 (20 mM HEPES pH 7.5, 0.5 mM spermidine, 0.1% Tween-20, 0.1% Triton X-100), nuclei were
1213 resuspended in calcium incubation buffer (3.5 mM HEPES pH 7.5, 10 mM $CaCl_2$, 0.1% Tween-
1214 20, 0.1% Triton X-100) and placed into an ice-cold block at 4 °C. MNase digestion was stopped
1215 by adding 100 µl of 2x Stop Buffer (340 mM NaCl, 20 mM EDTA, 5 mM EGTA, 0.1% Tween-
1216 20, 0.1% Triton X-100, 25 µg/ml RNase A, and 0.05 ng/100 µl E. coli spike-in DNA), followed by
1217 a 15 min incubation at 37 °C without shaking. Beads were then placed on a magnet and 200 µl of
1218 supernatant was collected. DNA was purified using the Zymo ChIP DNA Clean & Concentrator
1219 kit (D5205), eluted in 30 µl, and stored at −20 °C for library preparation. Libraries were generated

using the NEBNext Ultra II DNA library kit, quantified using a Qubit fluorometer with the HS DNA kit, checked for size distribution on the Agilent TapeStation, pooled equimolarly, and sequenced on an Illumina NovaSeq X.

Data analysis: Raw fastq files were aligned to the hg19 or mm10 genome using bowtie2 (v2.5.0)[102]. Low-quality reads were filtered using Samtools (v.1.9) with a MAPQ cut-off score of 30[103]. Only unique, deduplicated reads were retained for further processing. Bigwig files were produced using the deepTools package (v.3.5.1), using an ENCODE hg19 or mm10 v2 blacklist file to discard regions with consistently non-specific signal, and scaled using *E. coli* spike-in controls to normalize sequencing depth. To determine normalization factors based on *E. coli* reads, each sample was aligned to the *E. coli* genome (MG1655), and the unique deduplicated reads were compared across groups per antibody per experiment. The sample with the lowest number of *E. coli* reads was determined ("minimum"), and all samples were scaled by dividing their corresponding *E. coli* read count by this minimum number[104]. For each group, bigwig files were merged and peak callling was conducted using MACS2 (v2.1.0) with the corresponding merged IgG file as control, filtered for peaks with FDR < 0.05[105]. Peak annotation was conducted using HOMER (v4.1.1)[106]. Heatmaps were made either using the DiffBind (v3.8.4) or deepTools (v3.5.5) packages[53,107]. For deepTools, heatmaps were made by merging DEGs from RNA-seq data with TSSs downloaded from the UCSC genome browser using the canonically annotated transcript for each gene. Profiles were generated and statistically analyzed using the deepStats package[108] by using the dsCompareCurves function to perform Wilcoxon Rank-sum tests per-bin. For DiffBind analysis, heatmaps were made for peaks identified by DiffBind's differential peak algorithm, where differential peaks were first filtered using a $\log_2$(fold change) threshold > 0.1 and defined

at $p < 0.05$, where $\log_2$(fold change) was calculated as log2(parity) − log2(NP), based on prior empirical observations used to define thresholds for differential peaks[49]. ChEA analysis on annotated loci was conducted using EnrichR with a significance threshold of adjusted $p < 0.05$[109].

DATA AND MATERIALS AVAILABILITY

The genomics data generated in this study have been deposited in the National Center for Biotechnology Information Gene Expression Omnibus (GEO) database. We declare that the data supporting findings for this study are available within the article and Supplementary Information. Related data are available from the corresponding author upon reasonable request. No restrictions on data availability apply.

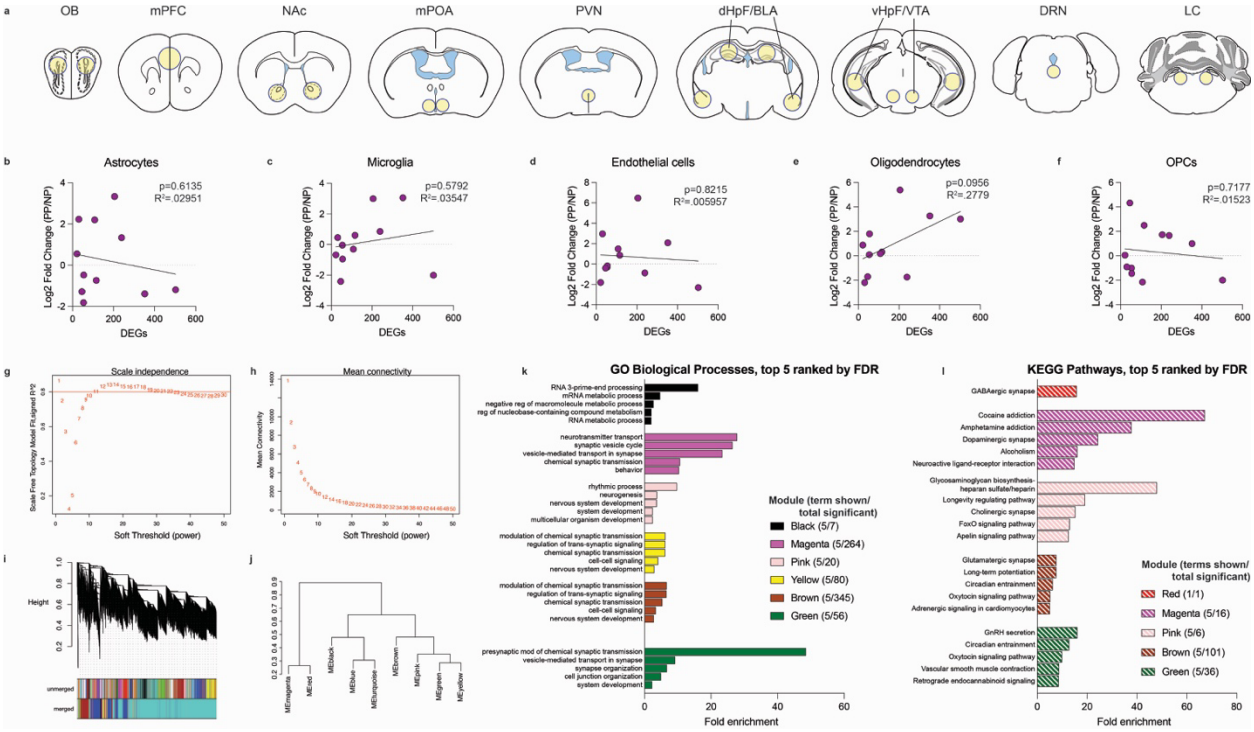

Extended Data 1: Brain-wide transcriptomic analysis of cell markers and gene expression networks. a) Brain regions selected for bulk transcriptional profiling: olfactory bulb (OB), medial prefrontal cortex (mPFC), nucleus accumbens (NAc), medial preoptic area (mPOA), paraventricular nucleus (PVN), dorsal hippocampal formation (dHF), basolateral amygdala (BLA), ventral hippocampus (vHF), ventral tegmental area (VTA), dorsal raphe nucleus (DRN), and locus coeruleus (LC). Yellow circles indicate area selected for tissue micropunching. **B-F)** Nonsignificant correlations between the fold change (NP *vs.* PP) in normalized surrogate proportion variables generated from cell-type deconvolution of bulk RNA-seq data for **B)** astrocytic, **c)** microglia, **d)** endothelial, **e)** mature oligodendrocyte, and **f)** oligodendrocyte precursor cell markers with the number of DEGs identified from each brain region. **g)** Scale independence plot for soft-threshold power selection for WGCNA analysis, illustrating the relationship between β and the scale-free topology fit index, identifying the optimal β value = 12. **h)** Mean connectivity plot illustrating the average network density for each evaluated soft-thresholding power. **i** Dendrogram of gene clustering based on topological overlap, highlighting the hierarchical clustering process used for module detection and merging of similar modules. **j)** Dendrogram of eigengene network adjacency depicting similarity of modules. **k, l)** Significantly enriched **k)** GO Biological Processes and **l)** KEGG pathways, sorted by FDR values, from module gene sets. Bars are color-coded to indicate modules. The total number of significant terms for each analysis is provided.

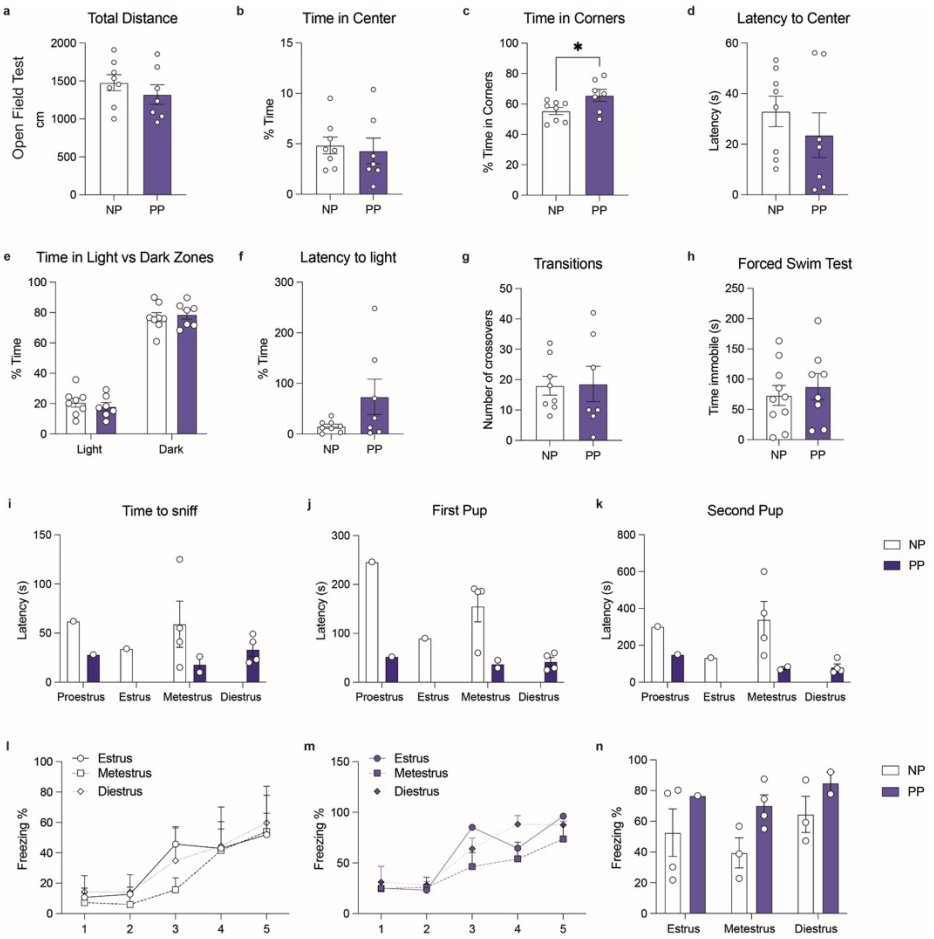

Extended Data 2: Parity associated behavioral adaptations are not influenced by locomotion, anxiety-/depressive-like behaviors, or estrous stage. a-d) In the open field test, there was no change in total distance, time spent in the center, or latency to the center. While there was a significant increase in time spent in corners for PP dams (Student's t-test, $t(13) = 2.307$, $*p = 0.0382$), this did not impact any other outcomes on the open field test. **e-g)** In the light-dark box, there was no difference in time spent in lights *vs.* dark zones, latency to enter the light zone, or transitions between zones. **h)** There was no difference in time spent immobile on the forced swim test. **i-k)** Stratification of pup retrieval behaviors by estrous stage on the day of testing did not reveal a significant effect of estrous stage. **l-n)** Similarly, stratification of contextual fear conditioning outcomes did not identify a significant effect of estrous stage on acquisition or context recall in NP or PP groups. Error bars represent mean ± SEM. N=6-11 animals/group.

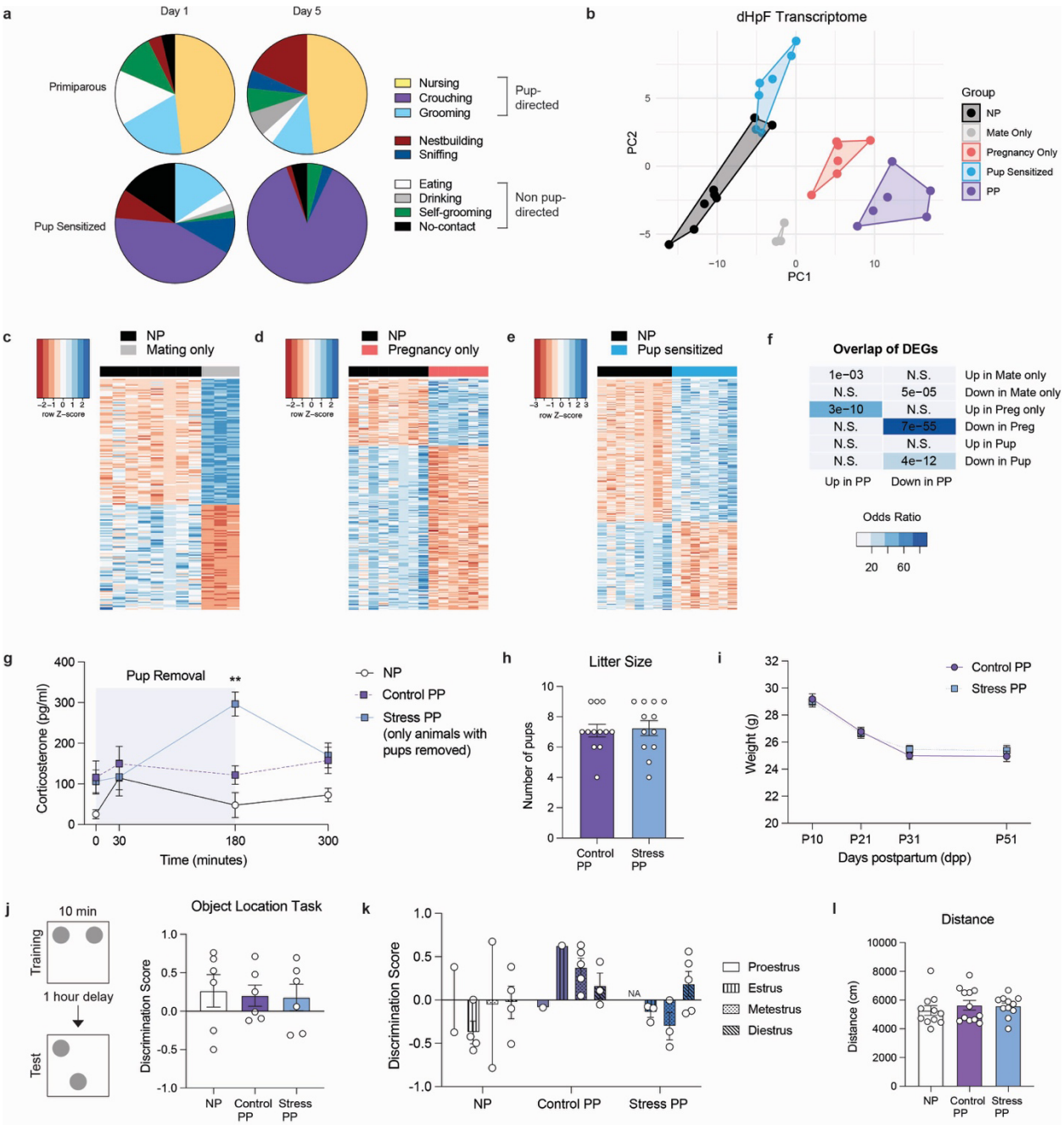

Extended Data 3: Postpartum experiences modulate the extent of parity-associated dHF transcriptomic and behavioral adaptations. a) Pie charts showing significant shifts towards pup-directed behaviors, representing maternal behavior initiation after four days of pup exposure in Pup Sensitized virgin females ($\chi^2(7) = 33.52$, $p = 2.11\text{x}10^{-5}$). **b)** Principle components analysis of NP *vs.* PP DEGs (adj $p < 0.05$) from dHF, showing the Pregnancy Only group clusters most closely with PP. **c)** Heatmaps of all significant DEGs comparing NP *vs.* Mating only, **d)** NP *vs.* Pregnancy only, **e)** NP *vs.* Pup sensitized dHF transcriptomes. **f)** Odds ratio analysis of DEG overlap for all comparisons (*vs.* NP). Insert numbers indicate respective *p* values for each association (N.S., $p > 0.05$). **g)** Pup separation increases maternal corticosterone levels over 3-hours (RM two-way ANOVA, group: $F(2,15) = 12.86$, $p = 0.0006$, time: $F(2.125, 31.87) = 2.759$,

1301 $p = 0.0756$, interaction: $F(6,45) = 3.294$, $p = 0.009$; Tukey's multiple comparisons test: Control
1302 *vs.* Stress PP, $^{**}p < 0.01$). N = 6 animals/group. **h)** No effect of postpartum stress on litter size. N
1303 = 12/group. **i)** Postpartum stress did not alter maternal weights. **j)** All groups discriminated the
1304 novel location following 10-minutes of training on the object location task (one way ANOVA,
1305 $F(2,15) = 0.06452$, $p = 0.9378$) N=6 animals/group. **k)** Stratification of object location test scores
1306 did not show a significant effect of estrous stage. **l)** There was no difference in the total distance
1307 travelled in the open field test across groups. Error bars represent mean ± SEM.
1308

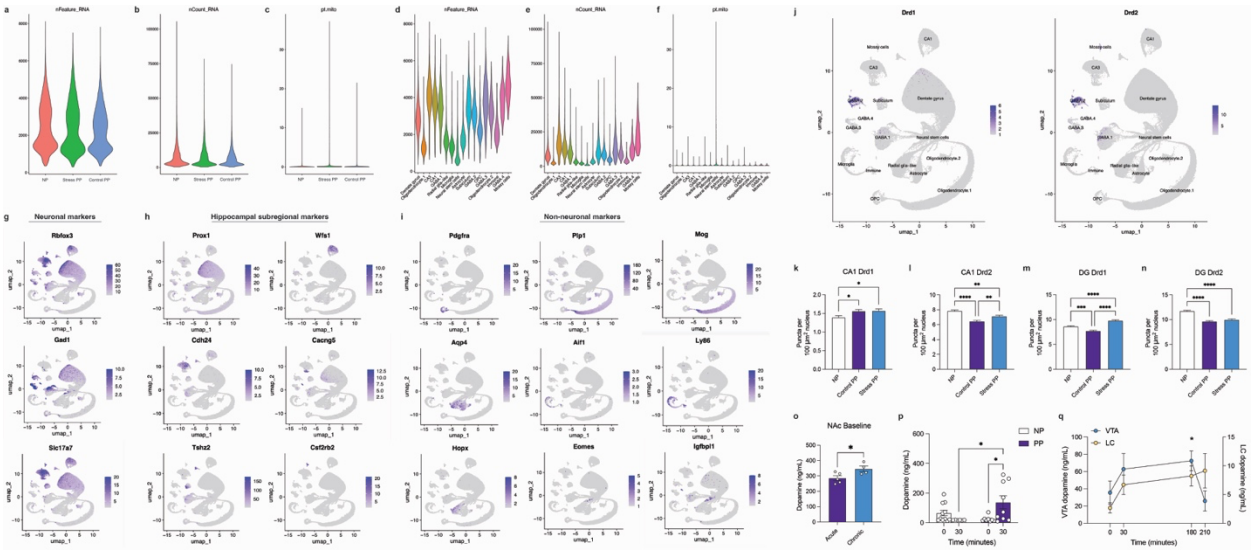

Extended Data 4: snRNA-seq quality control assessments, cell marker gene expression, and postpartum dopamine modulation. Violin plots showing the **(a)** number of detected genes, **(b)** UMI number, and **(c)** mitochondrial gene % by group following regression for mitochondrial gene mapping. (**d-f)** Breakdown of these metrics by annotated clusters show <10% mitochondrial gene across all cell-types, except for a minority of neural stem cells. Unsupervised clustering of snRNA-seq data with cells colored for **(g)** neuronal, excitatory, and inhibitory markers; **(h)** hippocampal subregional markers; and **(i)** non-neuronal markers including for glial and neural progenitor populations. **j)** Unsupervised clustering of snRNA-seq data with cells colored for *Drd1* (left) and *Drd2* (right) expression. **k)** Quantification of *Drd1* mRNA puncta in CA1 nuclei (one-way ANOVA, ($F(2,19204) = 3.963$, $p = 0.019$). **l)** Quantification of *Drd2* mRNA puncta in CA1 nuclei (one-way ANOVA, ($F(2,19204) = 23.16$, $p < 0.0001$). **m)** Quantification of *Drd1* mRNA puncta in dentate gyrus nuclei (one-way ANOVA, ($F(2,21864) = 42.09$, $p < 0.0001$). **n)** Quantification of *Drd2* mRNA puncta in dentate gyrus nuclei (one-way ANOVA, $(2,21864) = 41.79$, $p < 0.0001$). Tukey's multiple comparisons test, *$p < 0.05$, **$p < 0.01$, ***$p < 0.001$, ****$p < 0.0001$. **o)** Chronic postpartum stress resulted in higher baseline levels of dopamine in the nucleus accumbens (NAc; Student's t-test, $t(7) = 2.568$, *$p = 0.0371$). N= 4-5 animals/group. **p)** Dopamine response is not induced in NP dHF 30-minutes following littermate separation (two-way ANOVA, interaction of time x group ($F(1,30) = 8.78$, $p = 0.0059$, time ($F(1,30) = 1.47$, $p = 0.2359$, group, ($F(1,30) = 2.054$, $p = 0.1621$); Tukey's multiple comparisons test, *$p < 0.05$). N = 6-11 animals/group. **q)** Dopamine levels increased during pup separation in the VTA (left y-axis), but not in the locus coeruleus (right y-axis), resembling patterns of NAc and dHF dopamine dynamics (two-way ANOVA, effect of brain region ($F(1,46) = 32.32$, $p < 0.0001$), time ($F(3,46) = 2.311$, $p = 0.0866$), interaction ($F(3,46) = 1.118$, $p = 0.1109$); Dunnett's multiple comparisons test, *$p < 0.05$). N = 5-8 samples/group. Error bars represent mean ± SEM.

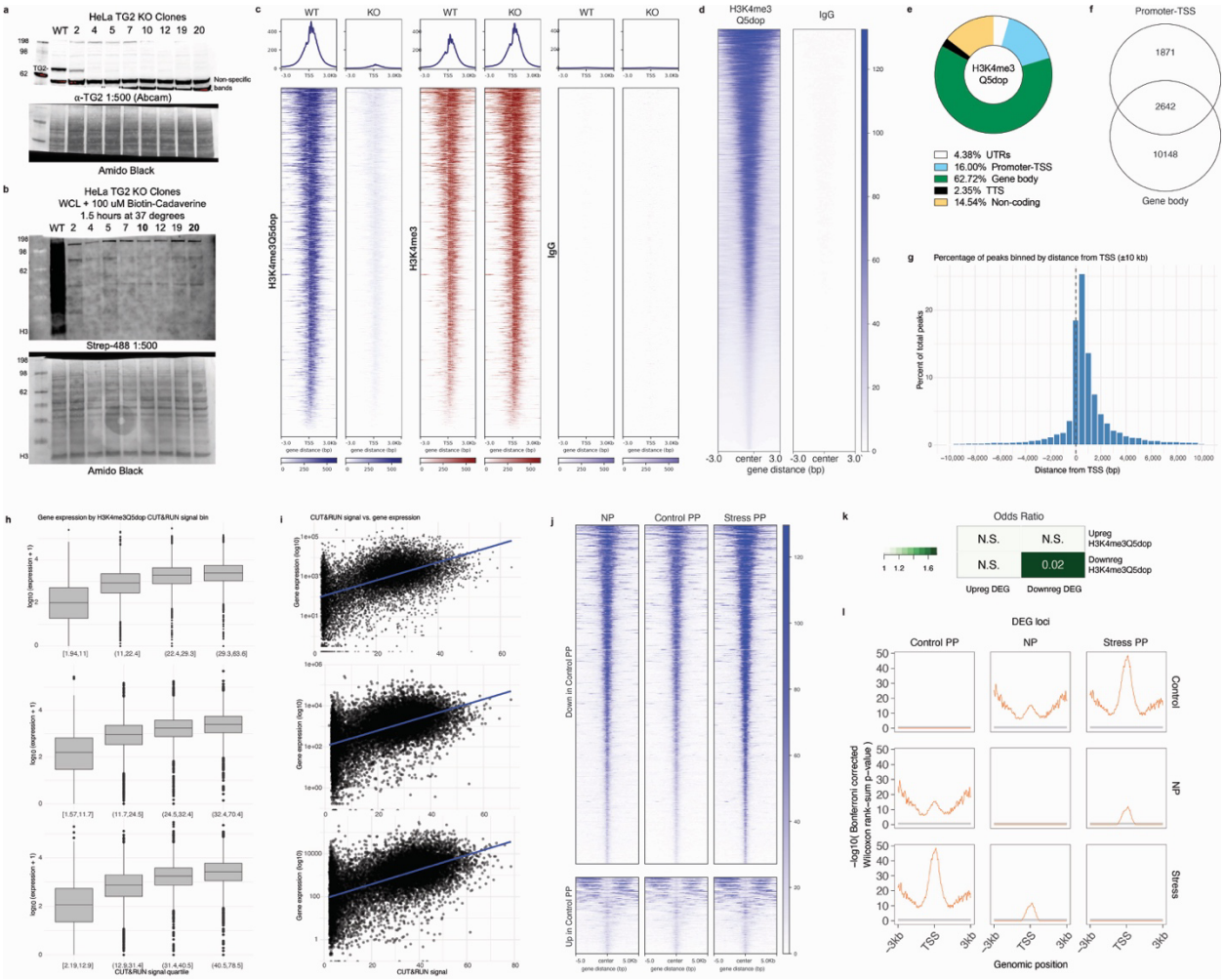

Extended Data 5: H3K4me3Q5dop enrichment corresponds with gene expression. a,b) Validation of TG2 knockout (KO) cell lines using **(a)** Western blot analysis to confirm the absence of TG2 protein, and **(b)** a transamidation activity assay to show loss of biotin-cadaverine incorporation in TG2 KO cells, indicating loss of enzymatic activity. **c)** TG2 KO results in a selective >90% reduction of H3K4me3Q5dop enrichment (*vs.* H3K4me3 alone) at transcription start sites (TSS) compared to WT controls. **d)** Heatmaps of H3K4me3Q5dop and IgG peak enrichment at all enriched loci in NP dHF tissue. **e)** Distribution of H3K4me3Q5dop enrichment occurs mainly at genic loci (83%), with **f)** overlap occurring between uniquely annotated promoter-TSS and gene body (exon/intron) regions and **g)** ~63.4% of total signal occurring within 2kB of the TSS. **h)** Boxplots displaying $\log_{10}$-transformed gene expression across quartiles of H3K4me3Q5dop signal for NP (top), Control PP (middle), and Stress PP (bottom). Significant differences were observed across bins (Kruskal–Wallis $p < 2.2 \times 10^{-16}$) for each group between each quartile. Boxes represent the interquartile range with the median indicated, and whiskers show the rangs with outliers plotted as individual points. **i)** Scatter plots showing the correlation between H3K4me3Q5dop CUT&RUN signal (maximum per gene) and mean gene expression ($\log_{10}$-transformed) for NP (top), Control PP (middle), and Stress PP (bottom). Significant positive correlations were observed for each group (NP: Spearman's $\rho = 0.55$, $p < 2.2 \times 10^{-16}$; Control PP: Spearman's $\rho = 0.52$, $p < 2.2 \times 10^{-16}$; Stress PP: Spearman's $\rho = 0.56$, $p < 2.2 \times 10^{-16}$), indicating

that increased H3K4me3Q5dop enrichment corresponds with higher transcriptional output. **j)** Heatmaps of all differential peaks ($p < 0.05$; $\log_2$FoldChange $\geq |0.1|$) between NP/Stress PP vs., separated by directionality and centered on genomic regions to show the majority of altered peaks decrease in Control PP dHF. **k)** Odds ratio analysis of differential H3K4me3Q5dop peaks and differentially expressed genes show significant association between downregulated histone dopaminylation and gene expression changes. Insert numbers indicate respective p values for each association (N.S., $p > 0.05$). **l)** Statistical comparison of H3K4me3Q5dop profiles across groups at loci associated with DEGs. Each panel shows the $-\log_{10}$ Bonferroni-corrected *p*-values from bin-wise Wilcoxon rank-sum tests comparing CUT&RUN signal across ±3 kb surrounding TSSs of DEG-associated loci. Comparisons are shown for each pairwise group contrast. Gray bars indicate bins that did not reach statistical significance after multiple hypothesis correction. The orange line reflects the statistical significance of signal differences across the TSS window, with higher values indicating greater confidence in differential enrichment between groups.

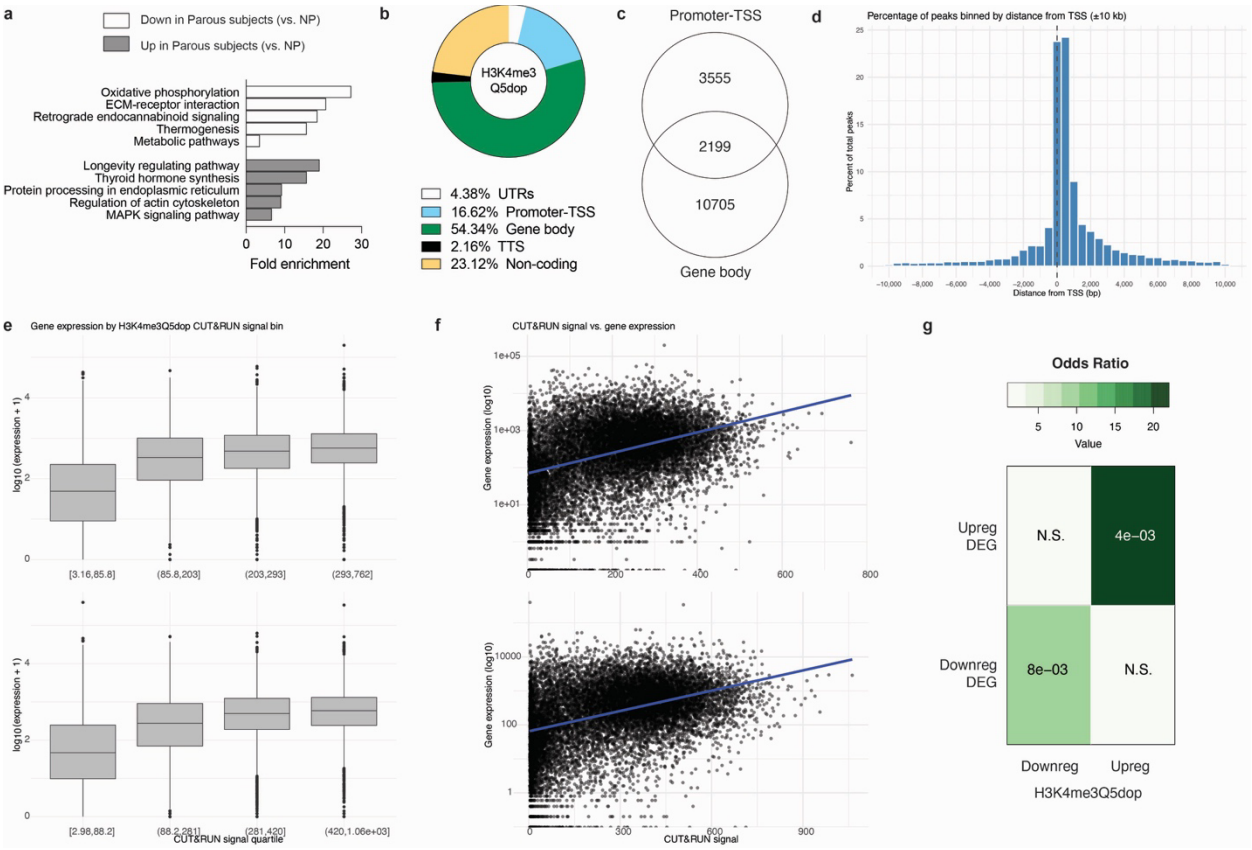

Extended Data 6: H3K4me3Q5dop enrichment in human brain. a) Pathway analysis for DEGs of NP vs. parous human dSub tissues by directionality (padj < 0.05). **b)** Distribution of H3K4me3Q5dop enrichment occurs mainly at genic loci (75.3%), with **c)** overlap occurring between uniquely annotated promoter-TSS and gene body (exon/intron) regions, similar to in mouse dHF, and **d)** ~52.0% of total signal occurring within 2kB of the TSS. **e)** Boxplots displaying $\log_{10}$-transformed gene expression across quartiles of H3K4me3Q5dop signal for NP (top) and parous subjects (bottom). Significant differences were observed across bins (Kruskal–Wallis $p < 2.2 \times 10^{-16}$) for each group and between each quartile. Boxes represent the interquartile range with the median indicated, and whiskers show the rangs with outliers plotted as individual points. **f)** Scatter plots showing the correlation between H3K4me3Q5dop CUT&RUN signal (maximum per gene) and mean gene expression ($\log_{10}$-transformed) for NP (top) and parous subjects (bottom). Significant positive correlations were observed for each group (NP: Spearman's $\rho = 0.41$, $p < 2.2 \times 10^{-16}$; Parous: Spearman's $\rho = 0.40$, $p < 2.2 \times 10^{-16}$), indicating that increased H3K4me3Q5dop enrichment corresponds with higher transcriptional output. **g)** Odds ratio analysis of differential H3K4me3Q5dop peaks and differentially expressed genes show significant association between changes in H3K4me3Q5dop signal and gene expression changes. Insert numbers indicate respective p values for each association (N.S., p > 0.05).

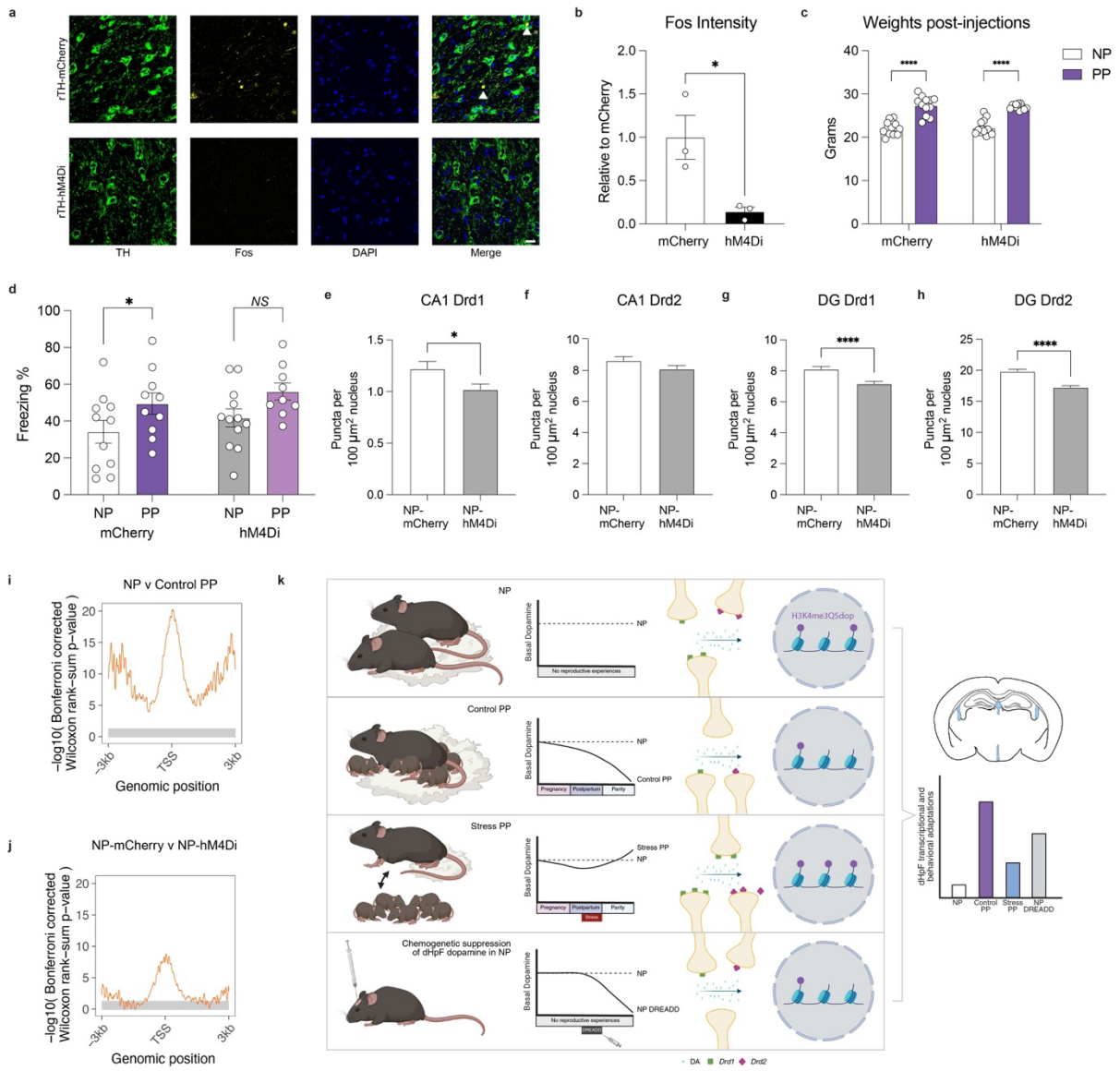

Extended Data 7: Inhibition of VTA-dHF projection mimics sustained changes in dopamine receptor dynamics. a) Representative images of c-Fos immunostaining in the VTA. Scale bars, 20 µm. **b)** Quantification of c-Fos immunoreactivity in VTA TH+ neurons (Student's t-test; t(4) = 3.299, *p = 0.03). N = 3 animals/group. **c)** Chronic DCZ injections did not alter weights at 21 dpp (two-way ANOVA; main effect of group (F(1,48) = 128, p < 0.0001), virus (F(1,48) = 0.0862, p = 0.7702); Tukey's multiple comparison's test, ****p < 0.0001). **d)** Parity induced significantly greater freezing on the context recall text in mCherry dams, with trending effects between hM4Di groups (two-way ANOVA (effect of group, (F(1,38) = 7.177, p = 0.0109, virus (F(1,38) = 1.631, p = 0.2093, Fisher's LSD, *p £ 0.05). N = 9-12/group. **e)** Quantification of *Drd1* mRNA puncta in CA1 nuclei (Student's t-test, (t(4854) = 2.249, *p = 0.00246). **f)** Quantification of *Drd2* mRNA puncta in CA1 nuclei (Student's t-test, (t(4854) = 1.502, p = 0.1132). **g)** Quantification of *Drd1* mRNA puncta in dentate gyrus nuclei (Student's t-test, (t(11946) = 3.900, ****p < 0.0001). **h)** Quantification of *Drd2* mRNA puncta in dentate gyrus nuclei (Student's t-test, (t(11946) = 6.034, ****p < 0.0001). **i, j)** Statistical comparison of H3K4me3Q5dop profiles between NP-mCherry

and NP-hM4Di at loci associated with **(i)** NP *vs.* Control PP DEGs and **(j)** NP-mCherry *vs.* NP-hM4Di DEGs. Each panel shows the $-\log_{10}$ Bonferroni-corrected *p*-values from bin-wise Wilcoxon rank-sum tests comparing CUT&RUN signal across ±3 kb surrounding TSSs of DEG-associated loci. Comparisons are shown for each pairwise group contrast. Gray bars indicate bins that did not reach statistical significance after multiple hypothesis correction. The orange line reflects the statistical significance of signal differences across the TSS window, with higher values indicating greater confidence in differential enrichment between groups. **k)** Schematic of working model.

REFERENCES

1. Hoekzema, E. *et al.* Pregnancy leads to long-lasting changes in human brain structure. *Nature neuroscience* **20**, 287–296 (2017).
2. Martínez-García, M. *et al.* Do Pregnancy-Induced Brain Changes Reverse? The Brain of a Mother Six Years after Parturition. *Brain sciences* **11**, 168 (2021).
3. Voldsbekk, I. *et al.* A history of previous childbirths is linked to women's white matter brain age in midlife and older age. *Human Brain Mapping* **42**, 4372–4386 (2021).
4. Pritschet, L. *et al.* Neuroanatomical changes observed over the course of a human pregnancy. *Nat Neurosci* 1–8 (2024) doi:10.1038/s41593-024-01741-0.
5. de Lange, A.-M. G. *et al.* Population-based neuroimaging reveals traces of childbirth in the maternal brain. *Proceedings of the National Academy of Sciences* **116**, 22341 LP – 22346 (2019).
6. de Lange, A.-M. G. *et al.* The maternal brain: Region-specific patterns of brain aging are traceable decades after childbirth. *Human Brain Mapping* **41**, 4718–4729 (2020).
7. Pawluski, J. L. & Galea, L. A. M. Hippocampal morphology is differentially affected by reproductive experience in the mother. *Journal of neurobiology* **66**, 71–81 (2006).
8. Duarte-Guterman, P. *et al.* Cellular and molecular signatures of motherhood in the adult and ageing rat brain. *Open Biology* **13**, 230217 (2023).
9. Workman, J. L. *et al.* Parity modifies the effects of fluoxetine and corticosterone on behavior, stress reactivity, and hippocampal neurogenesis. *Neuropharmacology* **105**, 443–453 (2016).
10. Macbeth, A. H., Scharfman, H. E., Maclusky, N. J., Gautreaux, C. & Luine, V. N. Effects of multiparity on recognition memory, monoaminergic neurotransmitters, and brain-derived neurotrophic factor (BDNF). *Hormones and behavior* **54**, 7–17 (2008).
11. Kinsley, C. H. & Lambert, K. G. Reproduction-Induced Neuroplasticity: Natural Behavioural and Neuronal Alterations Associated with the Production and Care of Offspring. *Journal of Neuroendocrinology* **20**, 515–525 (2008).
12. Barha, C. K., Lieblich, S. E., Chow, C. & Galea, L. A. M. Multiparity-induced enhancement of hippocampal neurogenesis and spatial memory depends on ovarian hormone status in middle age. *Neurobiology of Aging* **36**, 2391–2405 (2015).
13. Meurisse, M. *et al.* Estradiol receptor-α expression in hypothalamic and limbic regions of ewes is influenced by physiological state and maternal experience. *Hormones and Behavior* **48**, 34–43 (2005).
14. Love, G. *et al.* Maternal Experience Produces Long-Lasting Behavioral Modifications in the Rat. *Behavioral Neuroscience* **119**, 1084–1096 (2005).
15. Ammari, R. *et al.* Hormone-mediated neural remodeling orchestrates parenting onset during pregnancy. *Science* **382**, 76–81 (2023).
16. Leuner, B., Glasper, E. R. & Gould, E. Parenting and plasticity. *Trends in Neurosciences* **33**, 465–473 (2010).
17. Bridges, R. S. Neuroendocrine Regulation of Maternal Behavior. *Front Neuroendocrinol* **0**, 178–196 (2015).
18. McKenzie, A. T. *et al.* Brain Cell Type Specific Gene Expression and Co-expression Network Architectures. *Scientific Reports* **8**, 8868 (2018).
19. Paternina-Die, M. *et al.* Women's neuroplasticity during gestation, childbirth and postpartum. *Nat Neurosci* **27**, 319–327 (2024).

1461 20. Langfelder, P. & Horvath, S. WGCNA: an R package for weighted correlation network
1462 analysis. *BMC Bioinformatics* **9**, 559 (2008).
1463 21. Bridges, R. S. Long-term effects of pregnancy and parturition upon maternal
1464 responsiveness in the rat. *Physiology & Behavior* **14**, 245–249 (1975).
1465 22. Pawluski, J. L., Vanderbyl, B. L., Ragan, K. & Galea, L. A. M. First reproductive
1466 experience persistently affects spatial reference and working memory in the mother and
1467 these effects are not due to pregnancy or 'mothering' alone. *Behavioural Brain Research*
1468 **175**, 157–165 (2006).
1469 23. Pawluski, J. L., Walker, S. K. & Galea, L. A. M. Reproductive experience differentially
1470 affects spatial reference and working memory performance in the mother. *Horm Behav* **49**,
1471 143–149 (2006).
1472 24. Lemaire, V. *et al.* Motherhood-induced memory improvement persists across lifespan in
1473 rats but is abolished by a gestational stress. *The European journal of neuroscience* **23**,
1474 3368–3374 (2006).
1475 25. Gatewood, J. D. *et al.* Motherhood mitigates aging-related decrements in learning and
1476 memory and positively affects brain aging in the rat. *Brain research bulletin* **66**, 91–98
1477 (2005).
1478 26. Macbeth, A. H., Gautreaux, C. & Luine, V. N. Pregnant rats show enhanced spatial
1479 memory, decreased anxiety, and altered levels of monoaminergic neurotransmitters. *Brain*
1480 *research* **1241**, 136–147 (2008).
1481 27. Tomizawa, K. *et al.* Oxytocin improves long-lasting spatial memory during motherhood
1482 through MAP kinase cascade. *Nature Neuroscience* **6**, 384–390 (2003).
1483 28. Paris, J. J. & Frye, C. A. Estrous cycle, pregnancy, and parity enhance performance of rats
1484 in object recognition or object placement tasks. *Reproduction* **136**, 105–115 (2008).
1485 29. Stolzenberg, D. S. & Rissman, E. F. Oestrogen-independent, experience-induced maternal
1486 behaviour in female mice. *J Neuroendocrinol* **23**, 345–354 (2011).
1487 30. Cahill, K. M., Huo, Z., Tseng, G. C., Logan, R. W. & Seney, M. L. Improved identification
1488 of concordant and discordant gene expression signatures using an updated rank-rank
1489 hypergeometric overlap approach. *Scientific Reports* **8**, 9588 (2018).
1490 31. Fischer, D. S., Theis, F. J. & Yosef, N. Impulse model-based differential expression
1491 analysis of time course sequencing data. *Nucleic Acids Research* **46**, e119 (2018).
1492 32. McArdle, H. J. The metabolism of copper during pregnancy —a review. *Food Chemistry*
1493 **54**, 79–84 (1995).
1494 33. Leuner, B. & Sabihi, S. The birth of new neurons in the maternal brain: Hormonal
1495 regulation and functional implications. *Frontiers in neuroendocrinology* **41**, 99–113
1496 (2016).
1497 34. Lynch, M. A. Long-Term Potentiation and Memory. *Physiological Reviews* **84**, 87–136
1498 (2004).
1499 35. Le, A. A. *et al.* Prepubescent female rodents have enhanced hippocampal LTP and learning
1500 relative to males, reversing in adulthood as inhibition increases. *Nat Neurosci* **25**, 180–190
1501 (2022).
1502 36. Habib, N. *et al.* Div-Seq: Single-nucleus RNA-Seq reveals dynamics of rare adult newborn
1503 neurons. *Science* **353**, 925–928 (2016).
1504 37. Yao, Z. *et al.* A taxonomy of transcriptomic cell types across the isocortex and hippocampal
1505 formation. *Cell* **184**, 3222-3241.e26 (2021).

38. Gangarossa, G. *et al.* Characterization of dopamine D1 and D2 receptor-expressing neurons in the mouse hippocampus. *Hippocampus* **22**, 2199–2207 (2012).
39. Puighermanal, E. *et al.* Anatomical and molecular characterization of dopamine D1 receptor-expressing neurons of the mouse CA1 dorsal hippocampus. *Brain Struct Funct* **222**, 1897–1911 (2017).
40. Godino, A. *et al.* Dopaminoceptive D1 and D2 neurons in ventral hippocampus arbitrate approach and avoidance in anxiety. 2023.07.25.550554 Preprint at https://doi.org/10.1101/2023.07.25.550554 (2023).
41. Hansen, S., Bergvall, Å. H. & Nyiredi, S. Interaction with pups enhances dopamine release in the ventral striatum of maternal rats: A microdialysis study. *Pharmacology Biochemistry and Behavior* **45**, 673–676 (1993).
42. Champagne, F. A. *et al.* Variations in nucleus accumbens dopamine associated with individual differences in maternal behavior in the rat. *J Neurosci* **24**, 4113–4123 (2004).
43. Ford, C. P. The Role of D2-Autoreceptors in Regulating Dopamine Neuron Activity and Transmission. *Neuroscience* **282**, 13–22 (2014).
44. Farrelly, L. A. *et al.* Histone serotonylation is a permissive modification that enhances TFIID binding to H3K4me3. *Nature* **567**, 535–539 (2019).
45. Lepack, A. E. *et al.* Dopaminylation of histone H3 in ventral tegmental area regulates cocaine seeking. *Science* **368**, 197–201 (2020).
46. Zheng, Q. *et al.* Bidirectional histone monoaminylation dynamics regulate neural rhythmicity. *Nature* **637**, 974–982 (2025).
47. Chan, J. C. & Maze, I. Nothing Is Yet Set in (Hi)stone: Novel Post-Translational Modifications Regulating Chromatin Function. *Trends in Biochemical Sciences* **45**, 829–844 (2020).
48. Al-Kachak, A. *et al.* Histone serotonylation in dorsal raphe nucleus contributes to stress- and antidepressant-mediated gene expression and behavior. *Nat Commun* **15**, 5042 (2024).
49. Chan, J. C. *et al.* Serotonin Transporter-dependent Histone Serotonylation in Placenta Contributes to the Neurodevelopmental Transcriptome. *Journal of Molecular Biology* **436**, 168454 (2024).
50. Sardar, D. *et al.* Induction of astrocytic Slc22a3 regulates sensory processing through histone serotonylation. *Science* **380**, (2023).
51. Stewart, A. F., Lepack, A. E., Fulton, S. L., Safovich, P. & Maze, I. Histone H3 dopaminylation in nucleus accumbens, but not medial prefrontal cortex, contributes to cocaine-seeking following prolonged abstinence. *Mol Cell Neurosci* **125**, 103824 (2023).
52. Fulton, S. L. *et al.* Histone H3 dopaminylation in ventral tegmental area underlies heroin-induced transcriptional and behavioral plasticity in male rats. *Neuropsychopharmacology* **47**, 1776–1783 (2022).
53. Stark, R. & Brown, G. DiffBind: Differential binding analysis of ChIP-Seq peak data.
54. Shahrokh, D. K., Zhang, T.-Y., Diorio, J., Gratton, A. & Meaney, M. J. Oxytocin-Dopamine Interactions Mediate Variations in Maternal Behavior in the Rat. *Endocrinology* **151**, 2276–2286 (2010).
55. Pawluski, J. L., Lambert, K. G. & Kinsley, C. H. Neuroplasticity in the maternal hippocampus: Relation to cognition and effects of repeated stress. *Hormones and Behavior* **77**, 86–97 (2016).
56. Kinsley, C. H. *et al.* Motherhood Induces and Maintains Behavioral and Neural Plasticity across the Lifespan in the Rat. *Arch Sex Behav* **37**, 43–56 (2008).

1552 57. Jeffery, K. J. Integration of the sensory inputs to place cells: What, where, why, and how?
1553 *Hippocampus* **17**, 775–785 (2007).
1554 58. Lisman, J. E. & Grace, A. A. The Hippocampal-VTA Loop: Controlling the Entry of
1555 Information into Long-Term Memory. *Neuron* **46**, 703–713 (2005).
1556 59. Kimble, D. P., Rogers, L. & Hendrickson, C. W. Hippocampal lesions disrupt maternal, not
1557 sexual, behavior in the albino rat. *Journal of Comparative and Physiological Psychology*
1558 **63**, 401–407 (1967).
1559 60. Terlecki, L. J. & Sainsbury, R. S. Effects of fimbria lesions on maternal behavior in the rat.
1560 *Physiology & Behavior* **21**, 89–97 (1978).
1561 61. Numan, M. *et al.* The effects of D1 or D2 dopamine receptor antagonism in the medial
1562 preoptic area, ventral pallidum, or nucleus accumbens on the maternal retrieval response
1563 and other aspects of maternal behavior in rats. *Behav Neurosci* **119**, 1588–1604 (2005).
1564 62. Neukel, C. *et al.* The maternal brain in women with a history of early-life maltreatment: an
1565 imagination-based fMRI study of conflictual versus pleasant interactions with children. *J*
1566 *Psychiatry Neurosci* **43**, 273–282 (2018).
1567 63. Kim, P. *et al.* Perceived quality of maternal care in childhood and structure and function of
1568 mothers' brain. *Dev Sci* **13**, 662–673 (2010).
1569 64. Champagne, F. A. & Curley, J. P. Plasticity of the Maternal Brain Across the Lifespan:
1570 Plasticity of the Maternal Brain Across the Lifespan. *New Directions for Child and*
1571 *Adolescent Development* **2016**, 9–21 (2016).
1572 65. Deems, N. P. & Leuner, B. Pregnancy, postpartum and parity: Resilience and vulnerability
1573 in brain health and disease. *Frontiers in Neuroendocrinology* **57**, 100820 (2020).
1574 66. Dumais, A. *et al.* Risk factors for suicide completion in major depression: a case-control
1575 study of impulsive and aggressive behaviors in men. *Am J Psychiatry* **162**, 2116–2124
1576 (2005).
1577 67. Dumais, A. *et al.* Is violent method of suicide a behavioral marker of lifetime aggression?
1578 *Am J Psychiatry* **162**, 1375–1378 (2005).
1579 68. Mai, J. *Atlas of the Human Brain. 4th Ed.* (2016).
1580 69. Rice, C. J., Sandman, C. A., Lenjavi, M. R. & Baram, T. Z. A novel mouse model for acute
1581 and long-lasting consequences of early life stress. *Endocrinology* **149**, 4892–4900 (2008).
1582 70. Gilles, E. E., Schultz, L. & Baram, T. Z. Abnormal corticosterone regulation in an
1583 immature rat model of continuous chronic stress. *Pediatr Neurol* **15**, 114–119 (1996).
1584 71. Peña, C. J. *et al.* Early life stress confers lifelong stress susceptibility in mice via ventral
1585 tegmental area OTX2. *Science* **356**, 1185–1188 (2017).
1586 72. Fleming, A. S. & Rosenblatt, J. S. Maternal behavior in the virgin and lactating rat. *Journal*
1587 *of Comparative and Physiological Psychology* **86**, 957–972 (1974).
1588 73. Krishnan, V. *et al.* Molecular Adaptations Underlying Susceptibility and Resistance to
1589 Social Defeat in Brain Reward Regions. *Cell* **131**, 391–404 (2007).
1590 74. Champagne, F. A., Curley, J. P., Keverne, E. B. & Bateson, P. P. G. Natural variations in
1591 postpartum maternal care in inbred and outbred mice. *Physiology and Behavior* **91**, 325–
1592 334 (2007).
1593 75. Carcea, I. *et al.* Oxytocin neurons enable social transmission of maternal behaviour. *Nature*
1594 **596**, 553–557 (2021).
1595 76. Wolcott, N. S. *et al.* Automated classification of estrous stage in rodents using deep
1596 learning. *Sci Rep* **12**, 17685 (2022).

1597 77. Nagai, Y. *et al.* Deschloroclozapine, a potent and selective chemogenetic actuator enables
1598 rapid neuronal and behavioral modulations in mice and monkeys. *Nat Neurosci* **23**, 1157–
1599 1167 (2020).
1600 78. Secci, M. E., Reed, T., Quinlan, V., Gilpin, N. W. & Avegno, E. M. Quantitative Analysis
1601 of Gene Expression in RNAscope-processed Brain Tissue. *Bio Protoc* **13**, e4580 (2023).
1602 79. Bray, N. L., Pimentel, H., Melsted, P. & Pachter, L. Near-optimal probabilistic RNA-seq
1603 quantification. *Nature biotechnology* **34**, 525–527 (2016).
1604 80. Risso, D., Ngai, J., Speed, T. P. & Dudoit, S. Normalization of RNA-seq data using factor
1605 analysis of control genes or samples. *Nat Biotechnol* **32**, 896–902 (2014).
1606 81. Peixoto, L. *et al.* How data analysis affects power, reproducibility and biological insight of
1607 RNA-seq studies in complex datasets. *Nucleic Acids Res* **43**, 7664–7674 (2015).
1608 82. Love, M. I., Huber, W. & Anders, S. Moderated estimation of fold change and dispersion
1609 for RNA-seq data with DESeq2. *Genome Biol* **15**, 550 (2014).
1610 83. Ge, S. X., Jung, D. & Yao, R. ShinyGO: a graphical gene-set enrichment tool for animals
1611 and plants. *Bioinformatics* **36**, 2628–2629 (2020).
1612 84. Supek, F., Bošnjak, M., Škunca, N. & Šmuc, T. REVIGO Summarizes and Visualizes Long
1613 Lists of Gene Ontology Terms. *PLOS ONE* **6**, e21800 (2011).
1614 85. Krämer, A., Green, J., Pollard, J., Jr & Tugendreich, S. Causal analysis approaches in
1615 Ingenuity Pathway Analysis. *Bioinformatics* **30**, 523–530 (2014).
1616 86. Shen, L. GeneOverlap: An R package to test and visualize gene overlaps.
1617 87. Matevossian, A. & Akbarian, S. Neuronal Nuclei Isolation from Human Postmortem Brain
1618 Tissue. *J Vis Exp* 914 (2008) doi:10.3791/914.
1619 88. Hao, Y. *et al.* Integrated analysis of multimodal single-cell data. *Cell* **184**, 3573-3587.e29
1620 (2021).
1621 89. Young, M. D. & Behjati, S. SoupX removes ambient RNA contamination from droplet-
1622 based single-cell RNA sequencing data. *Gigascience* **9**, giaa151 (2020).
1623 90. McGinnis, C. S., Murrow, L. M. & Gartner, Z. J. DoubletFinder: Doublet Detection in
1624 Single-Cell RNA Sequencing Data Using Artificial Nearest Neighbors. *Cell systems* **8**,
1625 329-337.e4 (2019).
1626 91. Artegiani, B. *et al.* A Single-Cell RNA Sequencing Study Reveals Cellular and Molecular
1627 Dynamics of the Hippocampal Neurogenic Niche. *Cell Reports* **21**, 3271–3284 (2017).
1628 92. Zhou, Z., Zhi, C., Chen, D., Cai, Z. & Jiang, X. Single-nucleus RNA sequencing reveals
1629 cell type-specific transcriptome alterations of Down syndrome hippocampus using the
1630 Dp16 mouse model. *Genes Genomics* **45**, 1305–1315 (2023).
1631 93. Cembrowski, M. S., Wang, L., Sugino, K., Shields, B. C. & Spruston, N. Hipposeq: a
1632 comprehensive RNA-seq database of gene expression in hippocampal principal neurons.
1633 *eLife* **5**, e14997.
1634 94. Harris, K. D. *et al.* Classes and continua of hippocampal CA1 inhibitory neurons revealed
1635 by single-cell transcriptomics. *PLoS Biol* **16**, e2006387–e2006387 (2018).
1636 95. Haslinger, A., Schwarz, T. J., Covic, M. & Lie, D. C. Expression of Sox11 in adult
1637 neurogenic niches suggests a stage-specific role in adult neurogenesis. *Eur J Neurosci* **29**,
1638 2103–2114 (2009).
1639 96. Bandler, R. C. *et al.* Single-cell delineation of lineage and genetic identity in the mouse
1640 brain. *Nature* **601**, 404–409 (2022).
1641 97. Olney, K. C. *et al.* Widespread choroid plexus contamination in sampling and profiling of
1642 brain tissue. *Mol Psychiatry* **27**, 1839–1847 (2022).

1643 98. Xiang, M. *et al.* A Single-Cell Transcriptional Roadmap of the Mouse and Human Lymph
1644 Node Lymphatic Vasculature. *Front Cardiovasc Med* **7**, 52 (2020).
1645 99. Tasic, B. *et al.* Adult Mouse Cortical Cell Taxonomy by Single Cell Transcriptomics. *Nat*
1646 *Neurosci* **19**, 335–346 (2016).
1647 100. Miller, S. A. *et al.* LSD1 and aberrant DNA methylation mediate persistence of
1648 enteroendocrine progenitors that support BRAF mutant colorectal cancer. *Cancer Res* **81**,
1649 3791–3805 (2021).
1650 101. Skene, P. J. & Henikoff, S. An efficient targeted nuclease strategy for high-resolution
1651 mapping of DNA binding sites. *eLife* **6**, e21856 (2017).
1652 102. Langmead, B. & Salzberg, S. L. Fast gapped-read alignment with Bowtie 2. *Nat Methods* **9**,
1653 357–359 (2012).
1654 103. Li, H. *et al.* The Sequence Alignment/Map format and SAMtools. *Bioinformatics* **25**, 2078–
1655 2079 (2009).
1656 104. Qasim, M. N. *et al.* Genome-wide Profiling of Transcription Factor-DNA Binding
1657 Interactions in Candida albicans: A Comprehensive CUT&RUN Method and Data
1658 Analysis Workflow. *Journal of Visualized Experiments (JoVE)* e63655 (2022)
1659 doi:10.3791/63655.
1660 105. Zhang, Y. *et al.* Model-based Analysis of ChIP-Seq (MACS). *Genome Biology* **9**, R137
1661 (2008).
1662 106. Heinz, S. *et al.* Simple combinations of lineage-determining transcription factors prime cis-
1663 regulatory elements required for macrophage and B cell identities. *Mol Cell* **38**, 576–589
1664 (2010).
1665 107. Ramírez, F., Dündar, F., Diehl, S., Grüning, B. A. & Manke, T. deepTools: a flexible
1666 platform for exploring deep-sequencing data. *Nucleic Acids Res* **42**, W187-191 (2014).
1667 108. Gautier, R. gtrichard/deepStats: deepStats 0.3.1. Zenodo
1668 https://doi.org/10.5281/zenodo.3361799 (2019).
1669 109. Lachmann, A. *et al.* ChEA: transcription factor regulation inferred from integrating
1670 genome-wide ChIP-X experiments. *Bioinformatics* **26**, 2438–2444 (2010).
1671